https://doi.org/10.5194/egusphere-2026-6105
Preprint. Discussion started: 23 October 2026
© Author(s) 2026. CC BY 4.0 License.

PlanetScope Imagery for Slow-Moving Landslide Monitoring: Processing Strategies, Validation and Insight on Transient Processes

Laureen Maury[1], Joseph Huanca[1], Kevin Dhenin[1], Swann Zerathe[1], Franck Thollard[1], Luis Albinez[2], Dulio Gomez[2], and Pascal Lacroix[1]

[1]ISTERRE, Université Grenoble Alpes, Université Savoie Mont Blanc, CNRS, IRD, UGE, ISTerre, 38000 Grenoble, France
[2]INGEMMET, Lima, San Borja, Perú

Correspondence: Laureen Maury (laureen.maury@univ-grenoble-alpes.fr)

Abstract. Landslides can be affected by transient deformation, which can be difficult to measure, particularly for landslides in remote locations. Because these movements can be precursors to ruptures, monitoring landslides with high frequency satellite data is a key objective of research in mountain landslide hazards. The PlanetScope constellation, with a daily revisit frequency, has a demonstrated capability for tracking surface motion based on the correlation of image pairs. However, the results of the image correlations are affected by a series of artifacts coming from the acquisition geometry, acquisition timing, pair-choice strategy or type of matching algorithm. The choice of these strategies and algorithms has not been validated quantitatively by independent measurements from moving areas, and no integrated and validated workflow is yet available to process the whole chain of data. In this context, we propose an integrated, open-source, and containerized software for calculating displacement fields using PlanetScope imagery. We used several years of GNSS data from two monitored slow-moving landslides in Peru to evaluate the strategies of image pairing and correlation algorithms (block matching - BM and more global matching - MGM). We first show that commonly estimated errors on stable areas are substantially underestimating the errors on moving areas. We then show that the image acquisition timing within the day significantly impacts the results due to illumination effects. By combining these results, we show that both the BM and MGM algorithms can perform well, but the BM algorithm appears to be more effective at capturing fast-moving objects, while the MGM algorithm gives better results in low-velocity areas and reduces systematic errors. We also show the benefits of combining short-term pairs (<3 months) with long-term pairs (yearly) for a better mapping of transient movements. The strategies were applied to three Peruvian landslides and demonstrated that effective parameterization allows for the accurate capture of their transient spatio-temporal kinematic responses to three external forcing factors: fluvial erosion at the landslide toe, material supply from scarp retrogression, and earthquakes. These findings demonstrate the possibility and advantages of using PlanetScope's satellites for operational landslide monitoring and for studying internal mechanical interactions within slow-moving landslides.

1 Introduction

Landslides exhibit a wide range of velocities, from rapid and catastrophic events to slower deformation (Hungr et al., 2014). While rapid landslides involve rock, soil, and fluids moving at tens of meters per second, causing significant damage and casu-

https://doi.org/10.5194/egusphere-2026-6105
Preprint. Discussion started: 23 October 2026
© Author(s) 2026. CC BY 4.0 License.

alties (Froude and Petley, 2018), slow-moving landslides move at speeds between a few millimeters to a few meters per year (Lacroix et al., 2020b). They rarely cause fatalities, but continually threaten local communities by damaging infrastructure, causing loss of agricultural lands, and generating diverse socioeconomic impacts (Lacroix et al., 2020b). They can also evolve toward failure, acting as precursors of rapid land movements (Lacroix et al., 2020b). Therefore, it is crucial to identify these areas of slow deformation and track their activity over time, particularly since their frequency and occurrence will continue to increase as a result of urbanization, population expansion, agriculture and irrigation, and climate change (Guzzetti et al., 2012; Intergovernmental Panel On Climate Change (Ipcc), 2022, 2023; Narcisi et al., 2024), posing a serious threat to communities.

Remote sensing offers a valuable non-invasive method for landslide monitoring, enabling spatially continuous observation of surface displacements across large areas. Among remote sensing methods, optical satellite image correlation has emerged as a powerful tool for detecting and quantifying landslide motion (Delacourt et al., 2004; Leprince et al., 2008; Stumpf et al., 2017; Bontemps et al., 2018; Provost et al., 2022; Lacroix et al., 2022; Mueting and Bookhagen, 2024), particularly for large horizontal displacements where InSAR techniques often fail due to signal decorrelation or phase aliasing caused by acceleration (Handwerger et al., 2025). By comparing multi-temporal optical images, sub-pixel accuracy can be achieved to track ground movements even in complex topographic settings (Bontemps et al., 2018; Mueting and Bookhagen, 2024). The uncertainties of these correlation techniques are often estimated (Lacroix et al., 2022) as one-tenth of a pixel size for medium-resolution satellites, corresponding to approximately 1 m for Sentinel-2, 1.5 m for Landsat-8, and one-fifth of a pixel size for very high-resolution satellites (about 15 cm for Pléiades).

Since the 2000s, the era of regular high-frequency satellite acquisitions enabled a high revisit rate. Among these satellites, Sentinel-2, ASTER, and Landsat-8 provide a 10- to 25-year long-term archive every 5 to 16 days with a medium resolution (10 to 15 m pixel size). Since 2016, the PlanetScope constellation, composed of over 430 micro-satellites, or Doves, provides daily monitoring of Earth's surface with a resolution of approximately 3 m. The combination of high spatial and temporal resolution offers valuable opportunities for landslide studies (Frazier and Hemingway, 2021; Roy et al., 2021; Aati et al., 2022; Mueting and Bookhagen, 2024). In particular, several authors have demonstrated the ability of PlanetScope data to detect transient landslide motions. Bradley et al. (2019) used PlanetScope imagery to analyze landslides triggered by the 2018 Palu Valley earthquake, capturing detailed patterns of surface deformation linked to wet rice cultivation practices. Similarly, Mazzanti et al. (2020) demonstrated the utility of CubeSat-based PlanetScope data to monitor the Rattlesnake Hills landslide, highlighting their potential to track slow landslide displacement with high temporal resolution. Mueting and Bookhagen (2024) detected transient signals on the Siguas and Del Medio landslides. The high-frequency PlanetScope satellites also offer the potential to detect transient landslide motion prior to failure (Lacroix et al., 2023; Handwerger et al., 2025). While these results demonstrate the great potential of PlanetScope imagery, its use for displacement monitoring also presents significant technical challenges that must be addressed before it can be a reliable monitoring tool (Frazier and Hemingway, 2021; Aati et al., 2022; Mueting and Bookhagen, 2024; Mueting et al., 2026).

https://doi.org/10.5194/egusphere-2026-6105
Preprint. Discussion started: 23 October 2026
© Author(s) 2026. CC BY 4.0 License.

Several sources of error might impact image and correlation qualities, such as: outdated Digital Elevation Models (DEMs), acquisition geometry errors (Feng et al., 2019), striping effects (Kääb et al., 2017), and illumination variations. These different errors can be reduced by avoiding the selection of mosaic images or older images from PS2.SD (Dove-R) and PSD.SD (SuperDove) instruments (Aati et al., 2022), correlating pairs of images with minimal differences in acquisition geometry (viewing angles) (Mueting and Bookhagen, 2024), selecting pairs with similar illumination conditions (Mueting et al., 2026), and by using time-series inversion techniques that exploit the redundancy of PlanetScope image acquisitions (Dille et al., 2021; Lacroix et al., 2023). These different corrections have been applied using different strategies, for instance, using either long-term or short-term pairs (Mueting et al., 2026) or all the available pairs (Mueting and Bookhagen, 2024; Lacroix et al., 2023), or by using different correlation algorithms, including More-Global-Matching (MGM) and Block-Matching (BM) algorithms (Mueting and Bookhagen, 2024; Lacroix et al., 2023).

All these correction strategies have been evaluated by looking at systematic and random errors in the displacement estimates from correlation through first-order statistical metrics (e.g., RMSE or STD) on stable areas. However, an evaluation of the correction and correlation strategies has never been performed on active natural objects using independent datasets. Such an evaluation is, however, required to quantitatively compare the different processing strategies proposed and to define an optimized workflow that can be used for operational landslide monitoring. The development of this automatic and validated workflow becomes critical, given that images are available almost every day, and raises the issue of image quantity, storage resources, and processing time.

Integrating this context, our study aims (1) to combine existing pairwise PlanetScope corrections with time-series inversion for an optimal and open-source workflow of displacement time-series generation adapted to small objects like landslides (from a few hundred square meters to a few square kilometers), (2) to quantitatively compare the different pairing strategies and correlation algorithms by evaluating the results in diverse landslide environments, taking advantage of the frequent monitoring of different active landslides in Peru using campaign and permanent GNSS, and (3) to show the potential of the resulting time-series for analyzing the mechanics of landslides driven by rainfall, river erosion, earthquakes, and anthropogenic forcings.

2 Data and Methods

2.1 Study Sites

This study focuses on three active, slow-moving landslides in distinct regions of Peru: the Cajabamba landslide in Northern Peru, and the Pie de la Cuesta landslide (Vitor Valley) and Maca landslide (Colca Valley) in Southern Peru (Figure 1). The three landslides exhibit distinct land cover, controlling factors, and forcing factors, as well as diverse velocities. This diversity makes them ideal study sites for investigating the capacity of the PlanetScope satellite constellation to monitor landslide kinematics under different environmental conditions and observational configurations. GNSS data used in this study include both campaign-based measurements on the three landslide areas, as well as continuous recordings from permanent GNSS

https://doi.org/10.5194/egusphere-2026-6105
Preprint. Discussion started: 23 October 2026
© Author(s) 2026. CC BY 4.0 License.

stations installed as part of the joint INGEMMET-IRD Peruvian landslide monitoring observatory at Maca (Bontemps et al., 2020). These datasets were used to validate displacement time-series obtained from the PlanetScope images processing for Maca and Pie de la Cuesta. For the campaign measurements, dual-frequency differential GNSS receivers were employed using the Real-Time Kinematic (RTK) positioning technique. Various Trimble receiver models (R6-2, R7, R10, and R12) were used depending on availability and operability. This method provided horizontal precision with an average accuracy of approximately 1 cm (Figure 1). For Maca and Pie de la Cuesta, DEMs were obtained with Pleiades stereo images from 11/04/2022 and 08/10/2014, respectively, processed with Ames Stereo Pipeline (Beyer et al., 2018). The DEMs were sub-sampled to the same pixel size as the PlanetScope images (3 m). For Cajabamba, the DEM used comes from SRTM with a 30 meters resolution, resampled to a three-meter resolution to match the PlanetScope image resolution.

2.1.1 Maca Landslide

The Colca Valley, situated in the Central Andes, is a volcanic and seismically active zone. Its geology includes volcanic bedrock, lacustrine, and alluvial Quaternary deposits (Thouret et al., 2007). The thin lacustrine deposits are incised by the Colca River, which provokes several major deep-seated landslides (Pham et al., 2019). The Maca landslide, located on the left bank, affects an area of approximately 1.3 km^2 (Figure 1). Its volume is estimated to be around 60 to 100 million m^3, with a maximum depth of about 70 m. It is characterized by a semicircular head scarp and exhibits internal morphological features such as secondary scarps, fissures, and horst-and-graben-like structures (Zerathe et al., 2016). The landslide reactivation and motion are controlled by seasonal rainfall, seismic activity, and river erosion (Lacroix et al., 2014; Zerathe et al., 2016; Bontemps et al., 2020). Cumulative seasonal rainfall acts as the main forcing factor at the seasonal scale, while river erosion at the toe contributes over decades (Zerathe et al., 2016). The Maca landslide is also very sensitive to earthquakes, which can cause both co- and post-seismic displacements (Lacroix et al., 2014). Combined rainfall and seismic shaking lead to greater displacements than either factor alone (Bontemps et al., 2020). Over the past 30 years, the estimated velocity in the fastest-moving zone of the Maca landslide has been approximately 1.5 m/y (Bontemps et al., 2018). We focus our period of analysis between 25 April 2019 and 29 November 2021, during which eight GNSS campaigns were carried out to measure 11 markers (MA01 to MA11) (Figure 1B). In addition, the monitoring network includes two permanent GNSS stations, installed in late 2015 (MAD1 and MAD3), situated on the active landslide body. Continuous GNSS data from these stations, collected between 26 February 2019 and 30 December 2021 to coincide with the PlanetScope imagery, were processed using GAMIT/GLOBK v10.7 software, achieving subcentimeter precision.

2.1.2 Pie de la Cuesta Landslide

The Vítor Valley is a deeply incised, narrow valley that cuts northeast-southwest through the arid coastal plain of southwestern Peru (Vargas Vilchez, 1970) composed of detrital material with low cohesion. Situated at elevations over 1200 meters above sea level, between the foothills of the coastal mountain range and the western flank of the Andes (Figure 1), it features steep walls that can exceed 200 meters in vertical drop. Despite the dry environment, the valley is also prone to landslides, mainly triggered by irrigation-induced water infiltration (Lacroix et al., 2020a), among which the Pie de la Cuesta landslide is one of the most

https://doi.org/10.5194/egusphere-2026-6105
Preprint. Discussion started: 23 October 2026
© Author(s) 2026. CC BY 4.0 License.

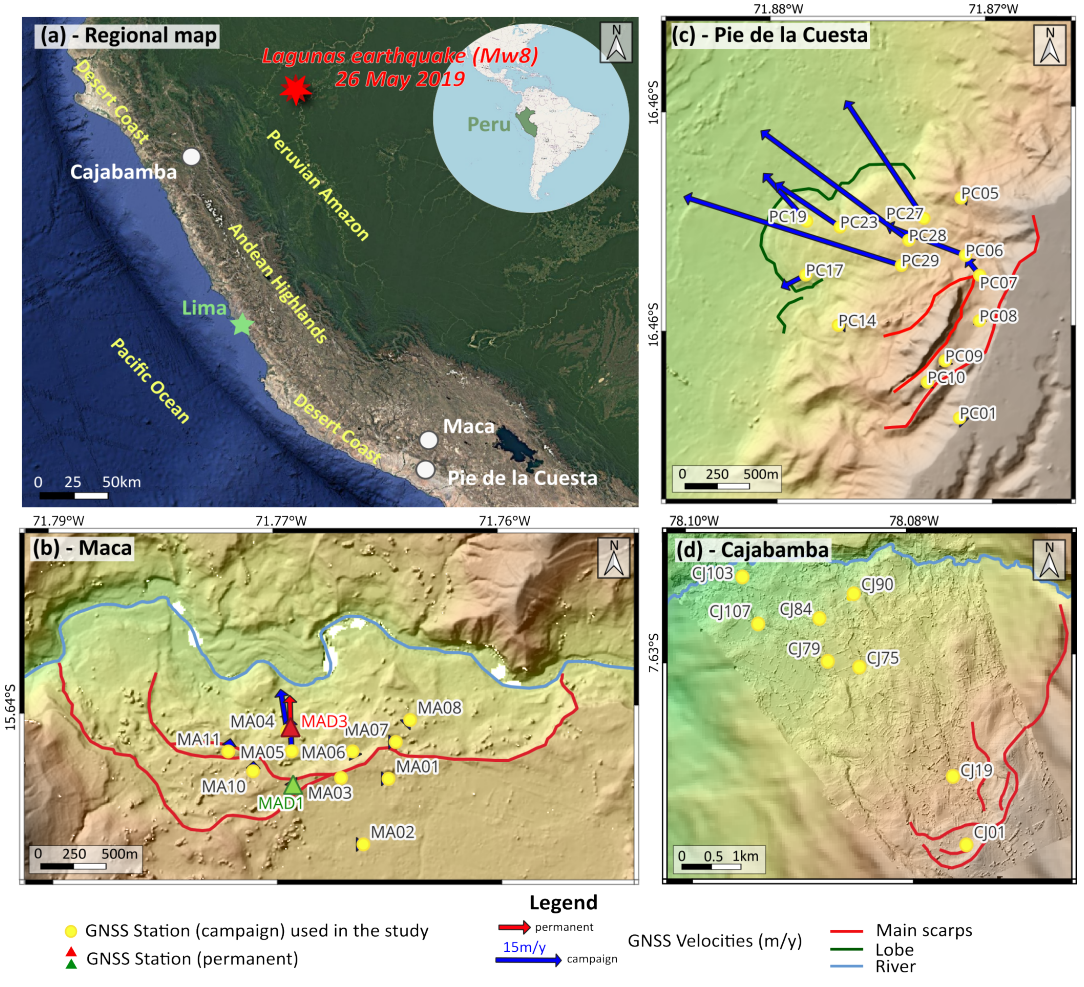


Figure 1. (a) Regional map showing the location of the three landslides (Imagery © 2021 Landsat/Copernicus and Open Street Map, Map data © 2026 Google, SIO, NOAA, U.S. Navy, NGA, GEBCO, LDEO-Colombia, NSF) . (b, c, d) Overview of the Maca Landslide, the Pie de la Cuesta landslide, and the Cajabamba Landslide. The velocity vectors are drawn for GNSS campaign points (in blue) and permanent GNSS stations (in red). The GNSS campaigns at Cajabamba were conducted during a period of no displacement; consequently, the velocity vectors are not represented.

active (Huayllazo et al., 2023; Infa et al., 2024). It is located on the left bank of the Vítor Valley (Figure 1), covering an area of approximately 0.6 km^2 and exhibiting complex movement types that include rotational sliding, falls, topples, and the formation of three main earth flows with lobular morphology at the toe. The head scarp is about 1.1 km long and up to 70 m high. The Pie de la Cuesta landslide has been active since its initial catastrophic failure on 9 January 1975 (Infa et al., 2024). In June 2016, the landslide entered a phase of increased activity marked by accelerated displacement (Lacroix et al., 2020a). The lithology of the Pie de la Cuesta landslide area consists of clays, gypsum, gravel conglomerates, tuffs, and weakly cemented Miocene alluvial deposits (Huayllazo et al., 2023). In particular, the presence of collapsible gravel conglomerates—quite cohesive when dry but

https://doi.org/10.5194/egusphere-2026-6105
Preprint. Discussion started: 23 October 2026
© Author(s) 2026. CC BY 4.0 License.

highly susceptible to strength loss upon water infiltration—has been identified as a key factor contributing to slope instability (Vargas Vilchez, 1970). A total of fourteen GNSS field campaigns were conducted at Pie de la Cuesta between 10 November 2017 and 19 November 2022 to measure the location of at least 28 markers, some of which were lost during periods of high activity followed by major remediation works. Velocities up to 4.5 m/month were indeed measured in this area in February 2022 (Instituto Geológico Minero y Metalúrgico, 2024).

2.1.3 Cajabamba Landslide

The valley of Cajabamba is situated on the right bank of the Rio Huamachuquino. It is composed of poorly compacted Quaternary fluvial sediments (clays, silty clays, and sandstones) as well as conglomerates, where water can easily infiltrate, preconditioning the slopes to a high susceptibility to mass movements (Nunez Juarez and Chacaltana Budiel, 2020). Heavy rainfall events (e.g., El Niño events) and earthquakes are the primary triggers of landslides in the region. On 26 May 2019, an Mw 8.0 earthquake struck the district of Lagunas, in the province of Alto Amazonas (Loreto, Peru). The event occurred at a depth of approximately 110 km, classifying it as an intermediate-depth earthquake. It was associated with normal faulting within the subducting Nazca Plate, inside the slab beneath the South American Plate (Vallée et al., 2023). The seismic waves propagated far to the west, impacting several regions, including the district of Cajabamba, 375 km from the epicenter, where pre-existing landslides (Figure 1) were reactivated (Nunez Juarez and Chacaltana Budiel, 2020). Cracks and subsidence processes have been recorded on agricultural fields. Following this earthquake, 107 GNSS markers were installed along the landslide and measured three times between 2022 and 2023. At Cajabamba, three GNSS campaigns were carried out on 07/06/2022, 25/10/2022, and 27/08/2023, a period during which the landslide was inactive.

2.2 PlanetScope Image Processing Implementation: the OCSlide workflow

By providing displacement maps that can be used to generate displacement time-series, the presented OCSLide workflow (Figure 2) aims to produce a spatial and temporal study of a slope deformation area. It follows a classical processing workflow based on the correlation of image pairs (Leprince et al., 2008; Beyer et al., 2018), error correction for each pair (Mueting and Bookhagen, 2024), and time-series inversion (Bontemps et al., 2018).

2.2.1 PlanetScope Images

PlanetScope is a commercial constellation of 430+ Dove and SuperDove satellites (CubeSat) managed by Planet Labs (Planet Labs, Inc., San Francisco, CA, USA). The satellites are in a low orbit (475–525 km). Thanks to this large constellation, it achieves a near-daily revisit time at nadir, making it an unprecedented tool for studying Earth's surface dynamics (Roy et al., 2021). PlanetScope data are acquired by three generations of sensors: Dove Classic, Dove-R, and SuperDove. The constellation has evolved through these three main satellite generations since July 2014: Dove-Classic (PS2), available from July 2014 to April 2022; Dove-R (PS2.SD), available from March 2019 to April 2022; and SuperDove (PSB.SD), launched in early 2020 and operational since mid-March 2020. These generations offer distinct spectral bands: PS2 with four bands (RGB-NIR),

https://doi.org/10.5194/egusphere-2026-6105
Preprint. Discussion started: 23 October 2026
© Author(s) 2026. CC BY 4.0 License.

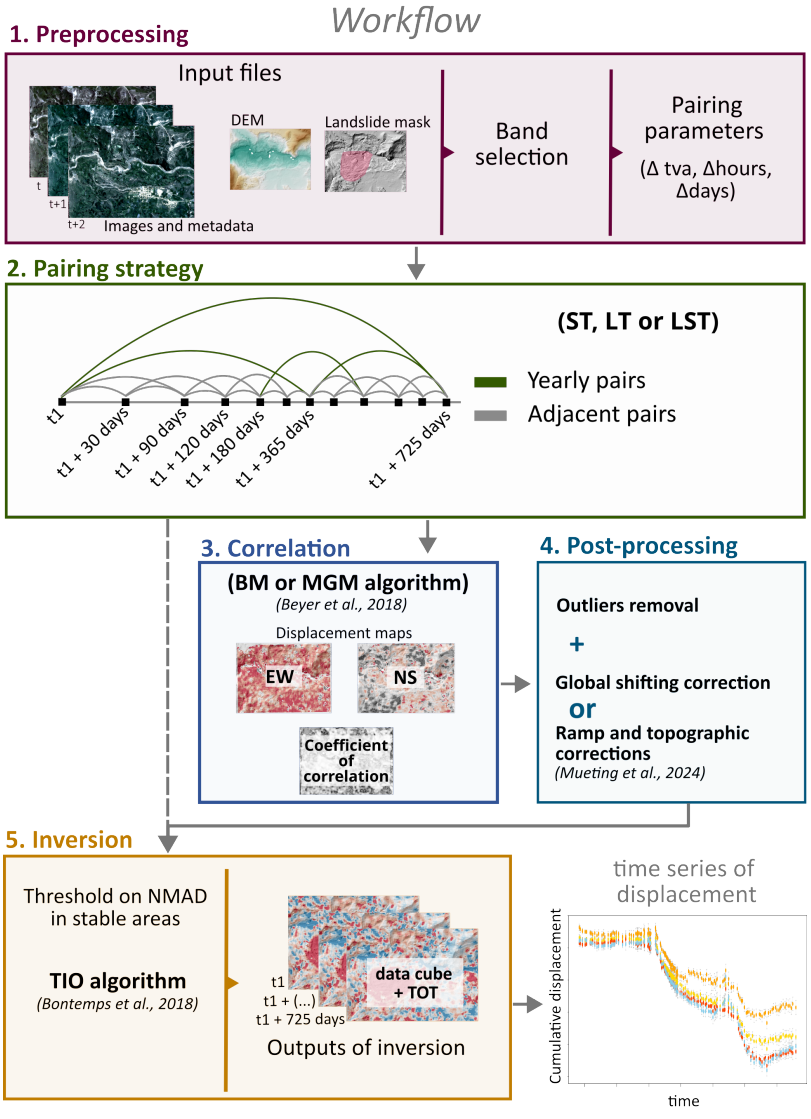


Figure 2. Presentation of the OCSLide workflow. (1) Formatting the input data (PlanetScope L3B images), selecting the parameters for correlations and pairing strategies, and extracting a single image band from the four available. (2) Creation of the pairing strategy based on the selected input parameters (ST, LT, or LST). (3) Correlation of each pair using either the Block Matching (BM) or the More Global Matching (MGM) method. (4) Corrections based on the NMAD threshold, which involve outlier removal based on the correlation coefficient, topographic correction (Mueting and Bookhagen, 2024), or simply centering based on the median value over stable areas. (5) Inversion of the pairs using the TIO algorithm—time-series Displacement Inversion from Optical Image Processing (Bontemps et al., 2018). The final outputs are cumulative displacement maps for each date, which can then be used to create time-series of displacement for specific locations.

PS2.SD with four improved bands (RGB-NIR), and PSB.SD with eight bands (coastal blue, blue, green I, green, red, yellow, red-edge, and NIR) (Mueting and Bookhagen, 2024). They are distributed in two processing levels: Level 1B (Basic Scene)

https://doi.org/10.5194/egusphere-2026-6105
Preprint. Discussion started: 23 October 2026
© Author(s) 2026. CC BY 4.0 License.

and Level 3B (OrthoScene). Level 1B products are calibrated and sensor-corrected but are not orthorectified; they provide Rational Polynomial Coefficients (RPCs) that enable users with advanced processing capabilities to perform their own custom orthorectification. Level 3B products are orthorectified by Planet, removing terrain distortions and projecting the images onto a cartographic coordinate system using Ground Control Points (GCPs) and Digital Elevation Models (DEMs) derived from various sources. Both L1B and L3B products are available at no cost but with a limited quota for university-affiliated researchers after registration, through Planet's Education and Research Program (Planet Labs PBS, 2023). While L3B is convenient for direct use, its geometric accuracy critically depends on the quality and accuracy of the DEM used in the orthorectification process (Aati et al., 2022; Mueting and Bookhagen, 2024).

The imagery is captured using push-frame satellite technology, where consecutive frames are collected and then stitched into

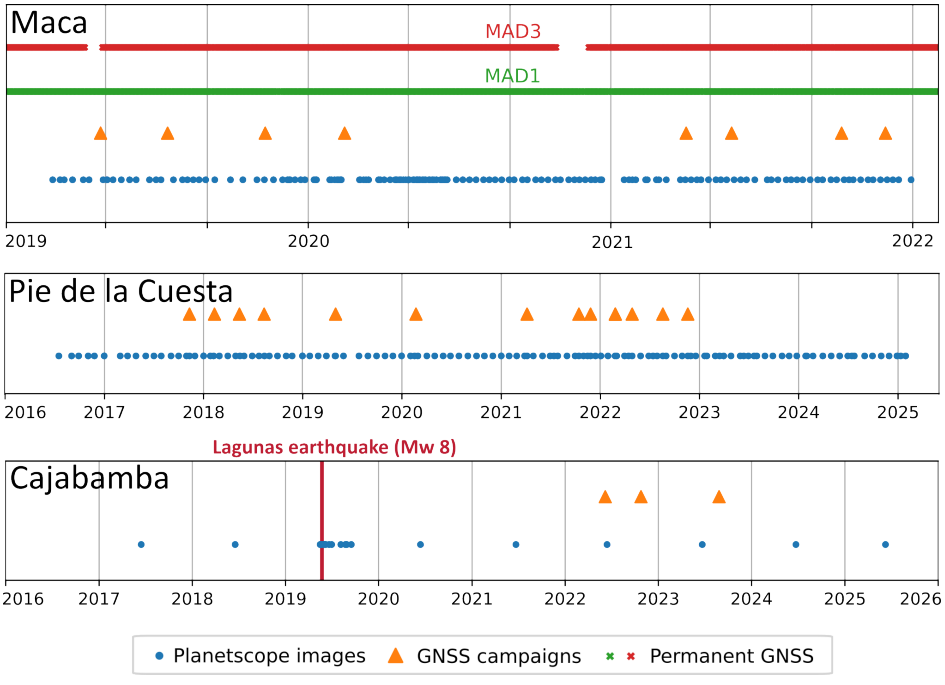


Figure 3. Timeline of PlanetScope imagery and GNSS data used in this study for the Maca, Pie de la Cuesta and Cajabamba landslides.

composite scenes. It is provided at a nominal 3 m spatial resolution (orthorectified pixel size), with a ground sampling distance (GSD) typically ranging from 3.7 m to 4.1 m. The approximate footprint (swath size) varies by sensor generation: PS2 scenes are around 24 km x 8 km, PS2.SD scenes are 24 km x 16 km, and PSB.SD scenes are 32.5 km x 19.6 km (Frazier and Hemingway, 2021; Mueting and Bookhagen, 2024). Key parameters characterizing image acquisition include the viewing angle (the spacecraft's across-track off-nadir angle), satellite azimuth (the spacecraft's off-track pointing direction, 0–360 degrees), which together define the satellite's perspective, and the hour of the day (local overpass time, most frequently around 10:03–10:29 AM in the study area), depending on the sensor generation (Roy et al., 2021).

https://doi.org/10.5194/egusphere-2026-6105
Preprint. Discussion started: 23 October 2026
© Author(s) 2026. CC BY 4.0 License.

As shown in Figure 3, 124 cloud-free PlanetScope images were visually selected in Pie de la Cuesta between 17/07/2016 and 29/01/2025, 153 images in Maca between 26/02/2019 and 30/12/2021, and 22 images in Cajabamba between 15/06/2017 and 09/06/2025. Image selection prioritized cloud-free conditions, spatial overlap with the Area of Interest (AoI), and the presence of stable reference zones. For analyzing specific transient events, higher revisit rates were required for Maca (up to 14 images per month were available in some periods of the year). For Cajabamba, the number of images is lower because the study focuses on the co- and post-seismic movements of the landslide following the Lagunas earthquake, which occurred on 26 May 2019. As a result, only one image per year was selected for the years between 2016 and 2025, specifically for the month of June. For 2019, 14 images were selected from May 17, 2019, to September 16, 2019.

2.2.2 Correlation

The correlation is based on pixel tracking in the AMES-Stereo Pipeline (Beyer et al., 2018), commonly used in the geoscience community due to its high parametrization capacity (Shean et al., 2016). Each pair is characterized by its ΔHours corresponding to the difference in the hour of the day between the two acquisitions; its ΔDate, corresponding to the difference in days between the two acquisitions; its ΔDays, corresponding to the number of days between the two acquisitions independent of the year (Julian day); and its Δtva, corresponding to the difference in True View Angle (tva) of the two acquisitions (Mueting and Bookhagen, 2024). The Δtva was computed using the following equation:

$$\Delta tva = \arccos\big(\sin(v_1)\sin(v_2)(\sin(a_1)\sin(a_2) + \cos(a_1)\cos(a_2)) + \cos(v_1)\cos(v_2)\big) \quad (1)$$

Where a1, a2 are the satellite azimuths and v1, v2 are the view angles for the two acquisition dates.

We tested two different algorithms commonly used by the community and implemented in the AMES-Stereo Pipeline software:

- Block Matching (BM) algorithm: The block matching algorithm is a local image correlation method that estimates displacement by comparing a correlation window centered on each pixel of the reference image with possible windows in the secondary image. A matching cost, typically based on normalized cross-correlation (NCC), is calculated to identify the best match (Beyer et al., 2018). The use of a restricted search region makes the method computationally efficient, particularly when the expected displacement can be estimated in advance. However, matching performance may decline in low-texture areas due to a lack of distinctive features (Facciolo et al., 2015). In this study, a fixed 21 × 21-pixel correlation kernel was used.

- More Global Matching (MGM) algorithm: The MGM algorithm is a global stereoscopic matching method based on semi-global matching (SGM) (Hirschmüller, 2008), which incorporates smoothness constraints between neighboring pixels to improve disparity estimation. By propagating information in multiple directions, MGM further constrains the disparity solution in low-texture regions and reduces trail artifacts (Facciolo et al., 2015; Purinton et al., 2023). MGM can therefore provide more reliable disparity estimates in low-texture regions. In this study, a fixed 7 × 7-pixel correlation kernel was used.

https://doi.org/10.5194/egusphere-2026-6105
Preprint. Discussion started: 23 October 2026
© Author(s) 2026. CC BY 4.0 License.

Each correlation generates three outputs: two maps of cumulative displacements along the East-West (EW) and North-South (NS) directions, as well as a map of correlation coefficients (CC) calculated over 21-pixel windows.

2.2.3 Post-correlation corrections

Outliers removal: A correlation coefficient (CC) threshold is applied to exclude unreliable pixels prior to any statistical analysis or correction, ensuring that only well-correlated regions are used. The temporal proximity of the images allows us to set this threshold at 0.2, which excludes only pixels with a very low correlation coefficient, ranging from 0 to 0.2, and preserves all pixels with a value greater than the threshold (0.2 to 1). The low value of the threshold was chosen to retain most of the pixels for each pair.

Global shifting, topographic, and ramp corrections: The Normalized Median Absolute Deviation (NMAD) is calculated over the stable zones to evaluate the correlation result. Stable zones are specified in relation to a manually built mask over the unstable area. If the NMAD is below a threshold (0.4 px in this study), only the median displacement is subtracted to remove potential global offsets. Otherwise, a correction for topographic and ramp errors is applied following a 2D (X,Y) linear regression, where an altitude term, Z, is added to subtract a planar ramp and a topographic correlation simultaneously. We followed the quadratic simplification used in Mueting and Bookhagen (2024), with a second-order polynomial equation:

$$aX_1^2 + bX_2^2 + cX_1X_2 + dX_1 + eX_2 + fZ + g \tag{2}$$

The adjustment simultaneously removes both ramp artifacts and global offsets (shifts). A moderate-resolution DEM (SRTM or GDEM) is sufficient to provide the altitude Z and correct for this topographic error.

2.2.4 Inversion and pairing strategies

The time-series inversion was performed with TIO (time-series displacement inversion from optical image processing) (Bontemps et al., 2018). This method assimilates all image pairs and reconstructs the displacement history that best explains the individual pairs using a least-squares strategy per pixel while minimizing the influence of noise and outliers. This method is coded in Fortran90 and has demonstrated its effectiveness in time-series of landslide motion measurements using a variety of optical satellites (Bontemps et al., 2018; Lacroix et al., 2019, 2020a, 2022; Provost et al., 2022). Given the large quantity of images, we define three different strategies for image pairing. The objectives are to evaluate each strategy's capacity to track displacement over time, select the appropriate pairs to minimize excessive redundancy if all available pairs were chosen, and maintain accuracy relative to the GNSS data as closely as possible. The three temporal strategies are:

- Short-term strategy (ST): Pairs of images were selected with short temporal baselines (less than 3 months), enhancing sensitivity to short-term or transient displacements. The nine images before and after a central image were used within an absolute time difference of 90 days.

https://doi.org/10.5194/egusphere-2026-6105
Preprint. Discussion started: 23 October 2026
© Author(s) 2026. CC BY 4.0 License.

- Long-term strategy (LT): Correlation of the three images before and after a central image within an absolute time difference of 90 days, as well as image pairs with a temporal separation of approximately one year (+/- 20 days), to preserve seasonal coherence.
- Long and Short-term strategy (LST): Combines the two approaches by selecting both the nine nearby images (within an absolute time difference of 90 days), as defined in the ST strategy, and the yearly pairs defined in the LT strategy.

The selection of image pairs is based on their limited time and date differences to avoid pairs acquired at different seasons, which exhibit lower correlation and a higher level of noise (Bontemps et al., 2018; Lacroix et al., 2019). This method limits the effects associated with illumination, which can create a sinusoidal signal in the time-series. Each strategy was tested with both the BM and MGM algorithms, resulting in six strategies tested independently on each landslide: BM + (ST, LT, or LST) and MGM + (ST, LT, or LST).Additional corrections were applied to correlated pairs that still exhibited high NMAD values. These pairs may degrade the quality of the inversion, and all pairs with NMAD values exceeding 0.7 m for Maca and 1 m for Pie de la Cuesta and Cajabamba were removed from the inversion pair list. We selected these thresholds by taking approximately ($\pm$1 standard deviation) the median of the NMAD values of all the pairs on the stable areas. The threshold value is determined by trial and error to ensure that the number of images removed is not excessive while eliminating outliers.

2.2.5 Maps and time-series of displacement

The results of the inversion consist of a data cube in which each band corresponds to an acquisition date and contains the displacement measured at each valid pixel. Displacements are provided separately in the East–West (EW) and North–South (NS) directions. By convention, positive displacement values correspond to motion toward the East in the EW direction and toward the South in the NS direction. Displacement time-series can be generated by extracting the displacement values at a given pixel through the sequence of displacement maps contained in the data cube. This allows the temporal evolution of displacement to be obtained for every valid pixel in the study area. In this study, the time-series presented for each measurement point were calculated by averaging the displacement values over a 9×9 pixel window centered on the selected pixel. This spatial averaging was used to maximize the coherence of the selected area and reduce the influence of outlier values, which may result from locally lower-quality correlations or less reliable displacement estimates.

The EW and NS displacement time-series can be projected onto the dominant local direction of motion, allowing the temporal evolution of displacement to be represented along the main direction. In addition, two parameters describing the spatial variability of velocity can be derived: the velocity gradient and velocity roughness. The velocity gradient describes the spatial rate of change in velocity, whereas velocity roughness characterizes local variations or irregularities in the velocity field. It is calculated by the largest inter-cell difference of a central pixel and its surrounding cell. Both parameters, calculated over a 3×3 kernel size, highlight spatial changes in deformation that may not be fully captured by velocity magnitude alone. Examining velocity gradient and roughness provides complementary information for assessing the spatial distribution of uncertainties and the reliability of the displacement estimates.

https://doi.org/10.5194/egusphere-2026-6105
Preprint. Discussion started: 23 October 2026
© Author(s) 2026. CC BY 4.0 License.

2.2.6 Open source automatic workflow

All steps of the workflow have been automated and containerized, and these have been validated with a workflow manager (Mölder et al., 2025). To ease the numerical processing of the data, we separated and isolated the different steps to make them idempotent. They can then be orchestrated by any workflow engine. Running experiments with a workflow engine allows for easy monitoring of the running experiments and automatically running only the necessary steps on changes (*e.g.*., when changing the algorithm or parameters). Among the plethora of workflow engines, we chose Snakemake (Mölder et al., 2025) as it is lightweight, easy to install and configure, and does not require admin privileges to be installed. We also provide a ready-to-use Singularity container that embeds all the dependencies and allows the workflow to run out of the box.

2.3 Validation on Peruvian Landslides

To validate the satellite-derived displacement time-series, we compared them with measurements from GNSS campaigns and continuous GNSS stations. To enable a direct comparison between the displacement variations derived from satellite observations and GNSS, we removed the initial offset from each time-series, as both methods provide relative displacements referenced to their own zero baselines. Different corrections to the vertical displacement values were then applied depending on the type of GNSS dataset (campaign or continuous):

- For GNSS campaign data, the nearest date in the satellite-derived displacement time-series was selected for each GNSS measurement, with a maximum tolerance of 30 days. The mean value of the 5 closest satellite dates is then compared to the GNSS value to realign the time-series and compare it to the GNSS values.
- For continuous GNSS (Maca), GNSS data served as the reference. A constant vertical shift is added to the satellite time-series to realign it with the GNSS time-series, minimizing the Root Mean Square Error (RMSE) between the two. Due to the inversion performed, satellite time-series may have an initial point other than zero, thus causing a disagreement between the GNSS and the satellite data.

This asymmetric treatment reflects the difference in temporal density: satellite time-series are denser than GNSS campaigns, while the opposite holds for continuous GNSS stations. The RMSE is used to validate the PlanetScope time-series. It evaluates errors in the satellite time-series relative to the time-series obtained from GNSS measurements.

3 Results

3.1 Satellite Acquisition Effects on Image Correlation

We tested the impact of the characteristics of the different image pairs (ΔHours, ΔDate, ΔDays, Δtva,) on the quality of the correlation for the three landslides (Figure 4). On the Pie de la Cuesta landslide, a total of 15,500 pairs were processed using images between 2016 and 2025. The NMAD values before corrections are distributed around a median value of 1.08 m. A clear

https://doi.org/10.5194/egusphere-2026-6105
Preprint. Discussion started: 23 October 2026
© Author(s) 2026. CC BY 4.0 License.

NMAD increase is observed for pairs involving the image from the 2nd of August 2016 at 19:25:07 UTC, which was acquired with a time difference of more than 3 hours relative to other images (pairs marked in green), highlighting the impact of illumination conditions associated with acquisition time. This underscores the critical role of shadows and solar angle variation in degrading correlation results. To limit this effect in our algorithm, we removed pairs acquired with ΔHours greater than 3 hours.

In contrast to a previous study (Mueting and Bookhagen, 2024), no clear trend is observed between the NMAD value and the difference in viewing angle between the two acquisitions (Δtva). This is caused by the evaluation of the NMAD on stable areas where topography does not change, so that DEMs are up to date. As suggested by Mueting and Bookhagen (2024), fixing the maximum Δtva in the choice of the pairs must certainly be considered in areas with strong changes in topography over time. When NMAD values are plotted against ΔDays, a distinct pattern emerges, especially in the NS component, where NMAD values form an arch-shaped curve, peaking near 180 days of separation. This pattern reflects seasonal changes in solar illumination, which alter shadow patterns and surface appearance across image pairs acquired six months apart. These effects are particularly noticeable in the NS direction due to PlanetScope's near-polar orbit, morning acquisition times, and seasonal variations in illumination, which can result in high sun azimuths and highlight north-facing slopes (Lacroix et al., 2019; Mueting and Bookhagen, 2024). In contrast, the EW component shows a more linear increase in NMAD with ΔDays, likely due to surface changes such as vegetation dynamics and agricultural activity in cultivated zones, as also previously noted by Bontemps et al. (2018). These changes accumulate over time and affect correlation, independently of illumination, as shown for the evolution of ΔDate. The superposition of both effects, illumination and terrain change, is especially noticeable in the NS component, where both seasonal signals and linear trends coexist. For the other two landslides, the same analysis has been carried out and shows similar results, in particular, the increase in NMADs as ΔDays increases and approaches 180 days. To limit this effect, our algorithm takes into account only yearly pairs with ΔDays less than 90 days.

3.2 Topographic and global shifting corrections

After the correlation stage, all pairs were corrected to remove global shifting or, if necessary, topography errors and ramp effects (see Section 2.2.3). Mean NMAD values obtained for each algorithm are shown in Table 1. For the MGM-ST strategy of the Pie de la Cuesta landslide, 1,338 pairs were corrected for global shifting (697 in EW and 641 in NS) and 194 for topographic and ramp effects (69 in EW and 125 in NS). For the pairs corrected for topographic and ramp effects, 98% showed an improvement in NMAD after applying the correction. The mean NMAD values of the improved pairs before correction were 1.49 m (EW) and 2.47 m (NS), which reduced to 0.60 m (EW) and 0.76 m (NS) after correction. The average relative gain, for all strategies, was 58.6% with some pairs reaching up to 80% improvement. For all strategies at Pie de la Cuesta, more pairs were corrected for global shifting than for topographic effects. The ramp and topographic corrections have reduced the NMADs by approximately 0.87 m (0.53 m for EW and 1.21 m for NS). The MGM algorithm achieves lower overall NMADs (0.79 m EW, 0.81 m NS) than those involving BM (1.64 m EW, 1.48 m NS).

https://doi.org/10.5194/egusphere-2026-6105
Preprint. Discussion started: 23 October 2026
© Author(s) 2026. CC BY 4.0 License.

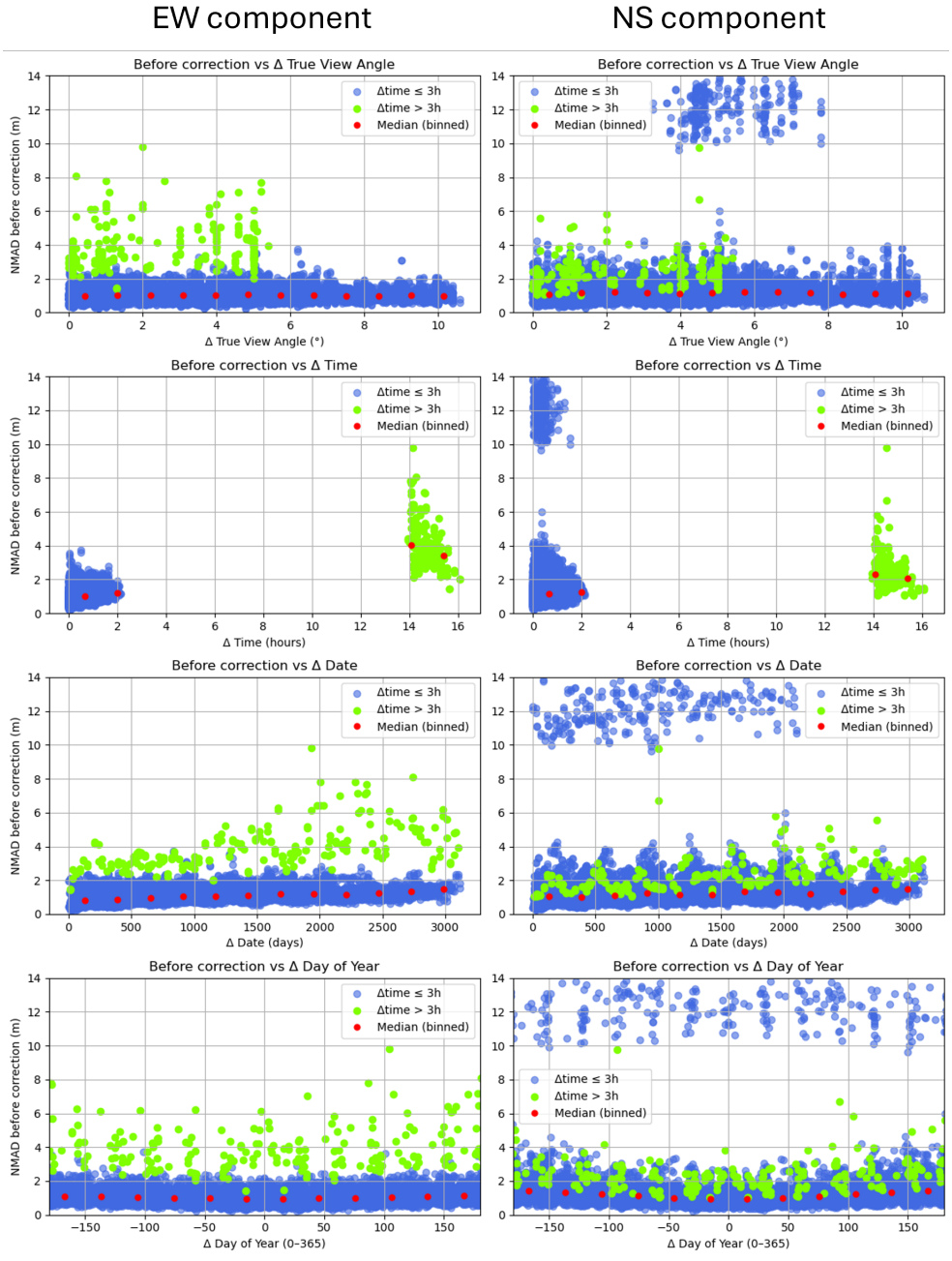


Figure 4. NMAD before correction vs Δtva, ΔHours, ΔDate, and ΔDays, between image pairs (for EW and NS components), realized for all pairs available for the Pie de la Cuesta landslide. For ΔDays, we plotted the difference in Julian days. The pairs marked in green have a ΔHours above three hours and show significantly high NMAD values.

https://doi.org/10.5194/egusphere-2026-6105
Preprint. Discussion started: 23 October 2026
© Author(s) 2026. CC BY 4.0 License.

Table 1. Mean NMAD values obtained for each algorithm (BM and MGM) over the three landslide areas (Pie de la Cuesta, Maca, and Cajabamba) and for the three pairing strategies (ST, LT, LST).

	Mean NMAD before corrections (m)				Mean NMAD after corrections (m)			
Algorithm	BM		MGM		BM		MGM	
Direction	EW	NS	EW	NS	EW	NS	EW	NS
Pie de la Cuesta	2.01	2.33	1.48	2.37	1.66	1.49	0.79	0.81
Maca	1.52	1.67	1.51	1.96	1.17	1.19	0.70	0.76
Cajabamba	1.70	1.45	1.57	1.42	1.04	0.95	0.73	0.69

For Maca, the NMADs remain low after corrections, with an average gain of 22% for strategies using BM and 52% for strategies using the MGM algorithm. As for Pie de la Cuesta, the NMADs are on average lower for MGM strategies (0.70 m for EW, 0.76 m for NS after corrections) than for BM strategies (1.17 m for EW, 1.19 m for NS after corrections). For Cajabamba, the same conclusions can be drawn. NMADs are generally slightly lower for strategies involving the MGM algorithm. After corrections, the NMADs are around 0.73 m EW and 0.69 m NS for the MGM strategies and 1.04 m EW and 0.95 m NS for the BM strategies.

3.3 Pair selection and threshold for inversion

Thresholds on Δtva, ΔHours, ΔDays, have been implemented in the workflow to carefully select the pairs to be correlated. These thresholds are set to limit the correlation between pairs that might be excessively affected by various errors discussed in (Mueting and Bookhagen, 2024) and in Section 3.1 of this study. In this study, Δtva is kept high enough to avoid reducing the number of pairs too much. ΔHours remains the same for all strategies, and ΔDays enables the differentiation of ST strategies from LT and LST strategies (Table 2).

For Pie de la Cuesta, with an initial number of 124 images, the total number of pairs that can be processed is 15,252 for each direction. The application of the different temporal strategies reduces this number to 766 for the ST strategy, 2,056 for the LT strategy, and 2,154 for the LST strategy. For Maca, 153 images were chosen over two and a half years, providing a high density of images per year. The number of possible pairs is 23,256. However, most pairs are not correlated due to the ΔDays threshold of 90 days. The LST strategies, which retain the most pairs, comprise 4,284 pairs. For Cajabamba, a total of 22 images were used, covering the period from 2016 to 2025, including 14 images in 2019, the year of the Lagunas earthquake, and one image per year otherwise. The ST strategies, which involve neighboring pairs, were not carried out. The maximum number of pairs that can be generated is 462. The threshold value for low-quality pairs after corrections was determined by trying different values manually to avoid removing many images while still eliminating outliers. In the end, the MGM algorithm allows more

https://doi.org/10.5194/egusphere-2026-6105
Preprint. Discussion started: 23 October 2026
© Author(s) 2026. CC BY 4.0 License.

Table 2. Number of images and pairs processed for each strategy on each landslide, before and after the application of the NMAD threshold ($NMAD_t$). The NMAD threshold ensures that only pairs with a low NMAD are retained for the inversion process. The thresholds are 0.7 m for the Maca landslide and 1.0 m for the Pie de la Cuesta and Cajabamba landslides.

Strategy		BM-ST		BM-LT		BM-LST		MGM-ST		MGM-LT		MGM-LST	
		Before $NMAD_t$	After $NMAD_t$	Before $NMAD_t$	After $NMAD_t$	Before $NMAD_t$	After $NMAD_t$	Before $NMAD_t$	After $NMAD_t$	Before $NMAD_t$	After $NMAD_t$	Before $NMAD_t$	After $NMAD_t$
Pie de la Cuesta	Images	124	124	124	123	124	123	124	124	124	123	124	123
	Pairs	766	616	2056	655	2154	678	766	616	2056	655	2154	678
Maca	Images	153	153	153	116	153	116	153	150	153	116	153	116
	Pairs	2634	1179	2846	511	4284	601	2634	1179	2846	511	4284	601
Cajabamba	Images	-	-	22	21	22	21	-	-	22	21	22	21
	Pairs	-	-	242	154	302	203	-	-	242	154	302	203

pairs to be retained by the threshold for inversion than the BM algorithm, due to the smaller NMADs over the stable areas of the MGM strategy (caused by the regularization of the MGM algorithm).

3.4 Validation of PlanetScope displacement using GNSS

We compare the time-series obtained from the six strategies against GNSS data collected from both permanent and campaign stations in the Maca and Pie de la Cuesta landslides to gain a better analysis of the uncertainties in the moving areas.

Figure 5 shows the NS (main direction of the movement) displacement time-series at the MAD3 permanent GNSS station in the Maca landslide, compared to the six strategies. Among them, the More Global Matching with Short-Term pairing (MGM-ST) performed slightly better, with an RMSE of 0.84 m, compared to 1.3 m for MGM-LT and 1.0 m for MGM-LST. The three MGM strategies worked better than the BM methods, which had larger errors, with RMSEs of 9.6 m, 9.5 m, and 6.2 m for BM-ST, BM-LT, and BM-LST, respectively, caused by a strong jump in the time-series at the end of 2019.

Adding long-term pairs aimed to reduce the errors by increasing the number of pairs. It also helps to better constrain periods of low displacement, for example, before the first acceleration of the landslide. We notice that for the MGM algorithm, long-term pairs also added a small bias during the second acceleration, in early 2021. Although the alignment with GNSS values is less accurate at the start of 2021, the three strategies using the MGM algorithm enable the different acceleration and deceleration phases of the landslide to be captured. When considering all GNSS stations, including both permanent and campaign measurements of the Maca landslide, the MGM-LST strategy has the best performance (Table 3), achieving the lowest average RMSE in EW (mean: 0.50 m; median: 0.49 m) and in NS (mean: 0.77 m; median: 0.45 m). The highest RMSEs were observed in high-velocity areas (e.g., MA04 and MAD3), while lower values generally occurred in low-velocity zones (e.g., MA03). In comparison, the BM algorithm produced higher and more variable errors, reaching up to 9.60 m (MAD3).

https://doi.org/10.5194/egusphere-2026-6105
Preprint. Discussion started: 23 October 2026
© Author(s) 2026. CC BY 4.0 License.

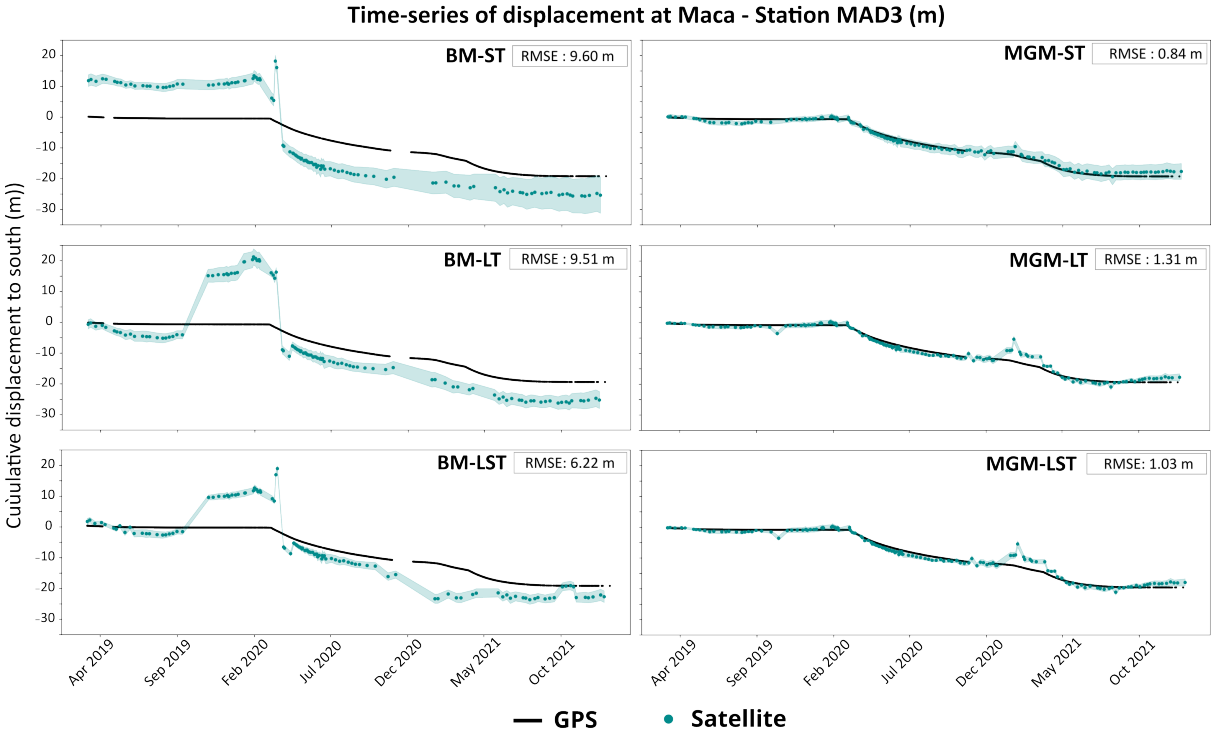


Figure 5. Displacement time-series on the Maca landslide obtained using six correlation strategies, combining three temporal baselines (short-term, long-term, and long-short-term) with two algorithms (More Global Matching and Block Matching). The results, derived from PlanetScope image correlation and time-series inversion, are compared against continuous GNSS measurements at the GNSS station MAD3 (see location in Figure 3). Each strategy reflects the impact of the correlation strategy on the agreement with GNSS data. The error bars for the six strategies displayed in the graph were calculated by computing the NMAD over stable terrain (Aati et al., 2022; Lacroix et al., 2023).

At Pie de la Cuesta, RMSE values were notably higher and spatially more heterogeneous than at Maca. The highest errors were observed under long-term correlation strategies, MGM-LT and BM-LT, with stations such as PC29 showing RMSE values exceeding 30 meters. In contrast, short-term strategies, BM-ST and MGM-ST, delivered better performance. The best-performing strategy, MGM-ST, produced the lowest median RMSE, with 1.36 m for the EW component and 1.14 m for the NS component. In both landslide cases, the MGM algorithm gives better overall results than the BM algorithm. Part of the difference is due to the smoothing performed by the MGM algorithm, which reduces local errors and results in generally lower NMAD values for MGM than for BM at similar velocities. However, as velocities increase, as is the case at Pie de la Cuesta where they reach several tens of meters per year, BM performs better than MGM. The NMAD values remain high for all strategies involving long pairs (LT and LST), regardless of the algorithm. This demonstrates the critical role of pair selection, which becomes more important than the choice of algorithm when high speeds are involved.

https://doi.org/10.5194/egusphere-2026-6105
Preprint. Discussion started: 23 October 2026
© Author(s) 2026. CC BY 4.0 License.

Table 3. Table of RMSE values for each tested pairing strategy compared with the corresponding GNSS measurement point for the Maca landslide. Measurements were taken between 2021 and 2022. The red boxes show the worst strategy (dark red) and the second worst (light red) strategy, while the blue boxes show the second-best (light blue) and the best (dark blue) strategy for each component and for each measurement point. RMSE values for Pie de la Cuesta are available in the supplements.

	NS Component (RMSE in meters)						EW Component (RMSE in meters)					
Measurement point	BM ST	BM LT	BM LST	MGM ST	MGM LT	MGM LST	BM ST	BM LT	BM LST	MGM ST	MGM LT	MGM LST
MAD1	1.30	0.69	0.84	1.05	0.81	0.84	0.41	0.57	0.58	0.56	0.66	0.65
MAD3	9.60	9.51	6.22	0.84	1.31	1.03	0.94	1.25	1.12	0.94	0.80	0.78
MA01	0.88	1.01	0.55	0.79	0.41	0.45	0.74	0.34	0.35	0.58	0.42	0.36
MA02	3.43	3.16	0.62	0.69	0.52	0.41	1.74	3.37	1.53	0.51	0.48	0.40
MA03	1.43	2.88	0.75	0.61	0.53	0.43	0.72	0.53	1.02	0.23	0.25	0.13
MA04	1.12	0.66	1.98	2.86	2.19	2.26	0.62	1.28	1.01	1.35	1.15	1.15
MA05	1.08	0.75	1.90	1.03	1.71	1.70	0.49	0.47	0.48	0.47	0.47	0.49
MA06	0.71	1.77	1.11	1.60	0.46	0.43	0.59	0.84	0.61	0.47	0.28	0.24
MA07	1.99	1.10	0.88	1.26	0.39	0.40	3.65	1.11	0.94	0.36	0.33	0.31
MA08	2.30	1.19	0.87	0.72	0.37	0.40	0.73	1.26	0.96	0.60	0.46	0.50
MA10	1.23	1.62	1.46	0.34	0.47	0.33	0.96	1.18	0.65	0.85	0.49	0.45
MA11	1.12	0.41	0.95	1.78	0.61	0.61	2.25	0.64	0.99	1.64	0.44	0.49
MEAN	2.18	2.06	1.51	1.13	0.82	0.77	1.15	1.07	0.85	0.71	0.52	0.50
MEDIAN	1.30	1.19	0.95	1.03	0.53	0.45	0.74	1.07	0.94	0.58	0.47	0.49

4 Discussion

4.1 Factors impacting the uncertainties

Thanks to GNSS validation, it is possible to identify the best-performing correlation strategy for each landslide: MGM-ST for Pie de la Cuesta and MGM-LST for Maca. Using these strategies, we evaluate the sources of error in the PlanetScope displacement time-series.

4.1.1 Seasonal effects through changes in illumination

By comparing the GNSS and satellite time-series, we notice that certain errors remain, particularly those related to changes in image illumination. This is illustrated by the velocity difference between GNSS station MAD3 and satellite data in Figure 6, for the MGM-ST and MGM-LST strategies. A persistent seasonal signal is observed in both strategies following the GNSS fit. The ST strategies, which are calculated using only short pairs, are more likely to develop this type of error. However, the persistence of this signal, even in strategies involving long pairs, is an error that needs to be better corrected. This shows that even by discarding pairs with strong illumination differences (acquisition time greater than 3 months or separated by more than 3 hours during the day), this effect remains. Correction of this effect will require further work and goes beyond the scope of this study. It is the subject of an ongoing study currently under review (Mueting et al., 2026).

https://doi.org/10.5194/egusphere-2026-6105
Preprint. Discussion started: 23 October 2026
© Author(s) 2026. CC BY 4.0 License.

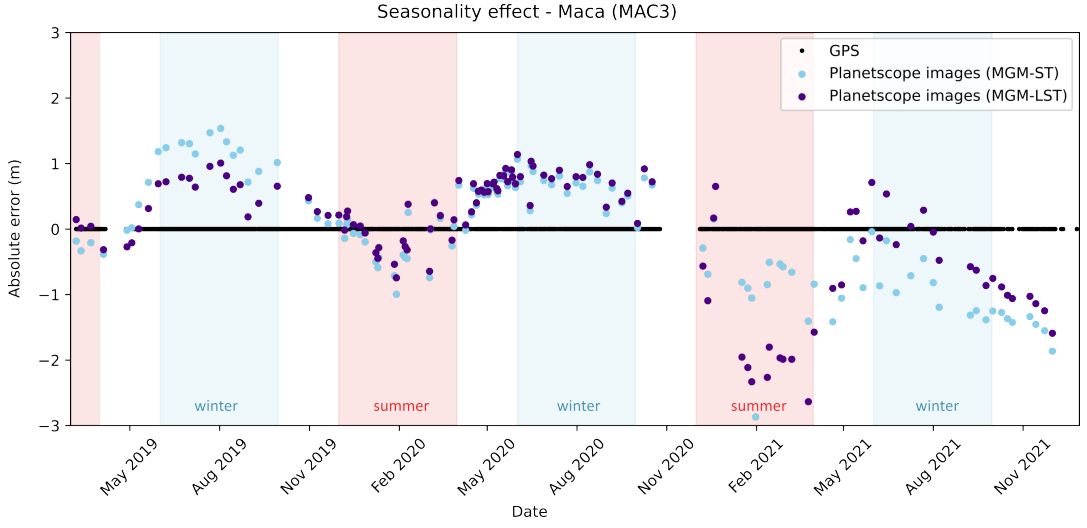


Figure 6. Seasonality effect. Graph showing the absolute error of the MGM-ST and MGM-LST strategies for the MAD3 permanent GNSS measurement point. Despite the fit, a seasonal signal persists due to changes in illumination throughout the year, leading to variations in light intensity.

4.1.2 Impact of the landslide velocity

The average velocity maps in Figure 7 illustrate the cumulative east-west velocity of the Pie de la Cuesta landslide over a period of approximately 8.5 years (July 2016 to January 2025), derived from PlanetScope image correlation using six different strategies. The velocity fields show that the short-term strategies (MGM-ST and BM-ST) are better at capturing the displacement of the landslide. The two strategies, MGM-LT and MGM-LST, show the largest deviation from the GNSS data and the reference strategy, which gives the lowest RMSE, the MGM-ST strategy. These two strategies are unable to track the large displacements in the central part of the landslide. For the BM-LT and BM-LST strategies, the results reveal the overall dynamics of the landslide. However, the results are lower in terms of velocity magnitude, and the edges of the landslide are not clearly mapped. These results suggest that velocity maps derived using the BM algorithm appear to be more strongly impacted by regions with high heterogeneity in the velocity field, such as transition zones between moving and stable areas.

The RMSE values are spatially heterogeneous (Figure 8), with lower errors concentrated in stable areas, such as the crown and flanks of the Pie de la Cuesta landslide, or low-velocity zones between the main scarp and the secondary scarp (graben-type block), and higher errors in high-velocity zones, like the central earth flow transport zones and lobes. This observation aligns with the understanding that uncertainties of correlation techniques are influenced by the spatial variability of ground kinematics within the correlation window used (Bontemps et al., 2018; Lacroix et al., 2019). For example, in Pie de la Cuesta, station PC29, located in a high-velocity sector, exhibits RMSE values exceeding 9 m in the EW component, while points like PC01, PC08, or PC09 in low-velocity sectors show RMSEs below 1 m.

https://doi.org/10.5194/egusphere-2026-6105
Preprint. Discussion started: 23 October 2026
© Author(s) 2026. CC BY 4.0 License.

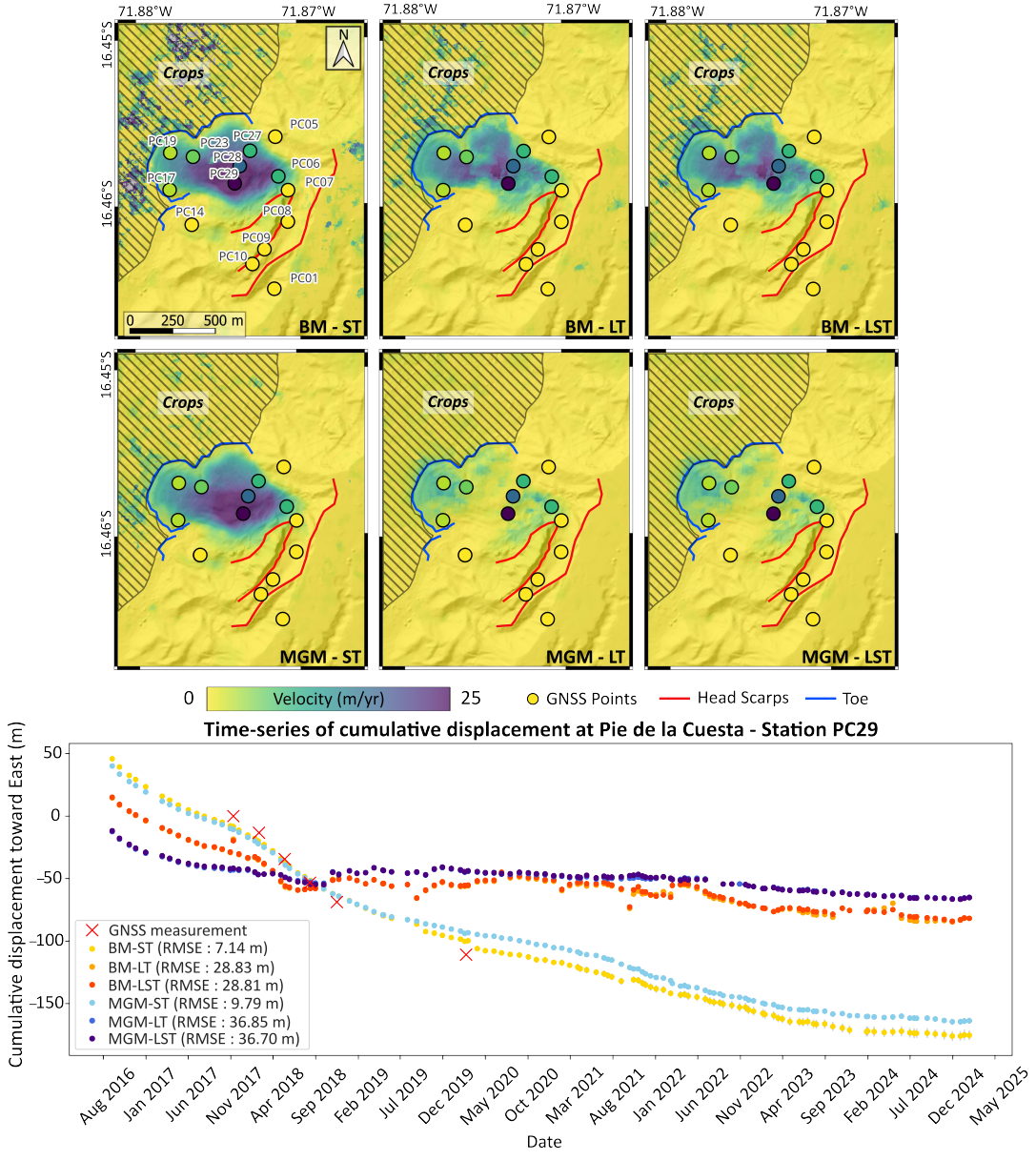


Figure 7. Velocities of the Pie de la Cuesta landslide between November 10, 2017, and November 19, 2022 (∼ 5 years), estimated using orthorectified PlanetScope L3B imagery. The six maps show velocity fields obtained with six correlation strategies combining three temporal baselines (short-term, long-term, and short-long-term) and two algorithms (More Global Matching – MGM, and Block Matching – BM). The color scale indicates the velocities in m/yr for the PlanetScope images and for the GNSS data. The time-series shows the cumulative displacement at station PC29, the station that experienced the highest velocity in the landslide. It highlights the underestimation of velocities obtained using the LT and LST strategies for both the BM and MGM algorithms.

https://doi.org/10.5194/egusphere-2026-6105
Preprint. Discussion started: 23 October 2026
© Author(s) 2026. CC BY 4.0 License.

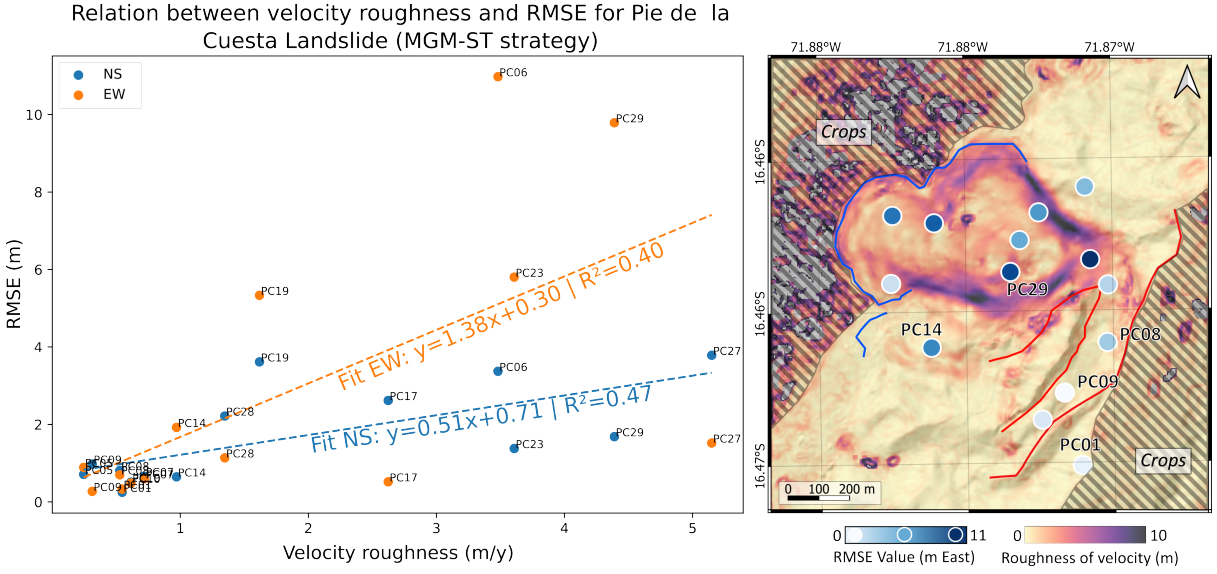


Figure 8. Relationship between the roughness of the velocity and RMSE values from PlanetScope image correlation for the East-West (EW) and North-South (NS) components at Pie de la Cuesta Landslide (a). (b) Map illustrating the MGM-ST strategy's roughness of velocity, where the highest RMSE values are found where the roughness is higher..

This relationship is explored in more detail in Figure 8, where the temporal RMSE computed at each GNSS station is plotted as a function of the spatial roughness of the velocity field, which measures the degree of spatial variability of the velocity field. Each point therefore represents a GNSS station, with its associated temporal RMSE compared to the local roughness of the surrounding velocity field. The plot highlights a general trend where higher roughness is associated with increased RMSE, reflecting challenges in correlation performance over fast-moving zones. This trend is observed for Maca and Pie de la Cuesta landslides and appears consistently in both displacement components. These results suggest that although the relationship between velocity and uncertainty is present in the four components, faster ground motion is associated with higher uncertainties. This is especially evident at Pie de la Cuesta, where the fastest GNSS station (PC29) experiences annual velocities exceeding 40 m/yr and RMSEs above 9 m (Figure 7). At Maca, although the maximum velocities are lower, the same trend is observed. For instance, station MA04 shows a velocity around 9 m/yr and RMSE values around 1.2 m, confirming that increased displacement rates tend to degrade correlation accuracy across landslides. The RMSE of the stable points varies considerably, with points such as PC01 (0.33 m for EW and 0.25 m) showing values well below the median (2.88 m for EW and 1.66 m), and points such as PC14 (1.92 m for EW and 0.65 m) having higher RMSEs.

Additionally, we evaluated the NMAD over stable areas outside the landslides. These regions, assumed to be unaffected by displacement, are often used to estimate the uncertainty in different studies (Bontemps et al., 2018; Lacroix et al., 2022). NMAD captures various sources of residual noise, including stereoscopic or topographic and ramp effects, and changes in

https://doi.org/10.5194/egusphere-2026-6105
Preprint. Discussion started: 23 October 2026
© Author(s) 2026. CC BY 4.0 License.

illumination conditions, which may induce seasonal biases in displacement estimates (Lacroix et al., 2023). For the Maca landslide, the More Global Matching with Long- and Short-Term pairing strategy (MGM-LST) generated not only the lowest RMSEs over the landslide (median values of 0.49 m for East-West (EW) displacement and 0.45 m for the North-South (NS) displacement) but also one of the lowest NMAD values in stable zones (0.71 m EW, 0.79 m NS). At Pie de la Cuesta, for the chosen strategy (MGM-ST), which was observed to be efficient for high-velocity areas (as well as BM-ST), the average NMAD values (0.60 m EW and 0.76 m NS) were the lowest compared to other strategies' average NMADs (1.28 m EW and 1.20 m NS for strategy BM-ST).

In conclusion, uncertainty estimation depends on the object's velocity and the spatial heterogeneity of the velocity, and estimating uncertainty in stable regions may greatly underestimate the uncertainties in moving areas.

4.1.3 Impact of surface changes on the results quality

Surface changes such as fracturing, landslide tilting, and modifications in vegetation or land cover have been shown to introduce noise in the correlation process (Bontemps et al., 2018; Mazzanti et al., 2020). In the case of Pie de la Cuesta, anthropogenic activity plays an additional role. Short-term strategies showed significantly better results than LT and LST strategies. When examining the individual correlations, a time-related decorrelation can be observed in the landslide data. Correlations involving images classified as short pairs, i.e., with a ΔDays of less than 3 months, show better results than the longer pairs, known as yearly pairs, involved in the LT and LST strategies. The decorrelated areas increase with the ΔDate and appear to be associated, in the lower part, with construction work and new roads being built to continue allowing vehicles to pass through (Figure 9).

In the upper part of the landslide, the construction of a road between 2019 and 2020 cannot alone explain the entire decorrelated area. In this part of the landslide, as shown by the PlanetScope images and those available on Google Earth, there were numerous morphological changes on the surface of the landslide due to secondary scarps, as well as rockfalls within the landslide mass. Furthermore, the correlation windows used in MGM (7x7px) and BM (21x21px) may be a limiting factor in tracking the very fast movements of Pie de la Cuesta in this area, where velocities can exceed 45 m/yr. In addition, the high velocity causes significant surface changes, which may increase image decorrelation.

Moreover, when we consider the inaccuracies that may be caused by the presence of clouds or snow in the images, it becomes clear how essential it is to select the images carefully. This shows that a careful selection of the images is required and that temporal decorrelation must sometimes be considered either by a ST strategy or weights added to LT pairs, as done in Bontemps et al. (2018) or Lacroix et al. (2019).

The current analysis tested short-term (up to 9 adjacent images) and long-term (3 adjacent images +/- multiple years) image pairings independently. Each of these strategies presents advantages: short-term strategies improve image similarity and spatial coherence, while long-term pairings capture seasonal motion and reduce inversion artifacts over slowly deforming zones. LST

https://doi.org/10.5194/egusphere-2026-6105
Preprint. Discussion started: 23 October 2026
© Author(s) 2026. CC BY 4.0 License.

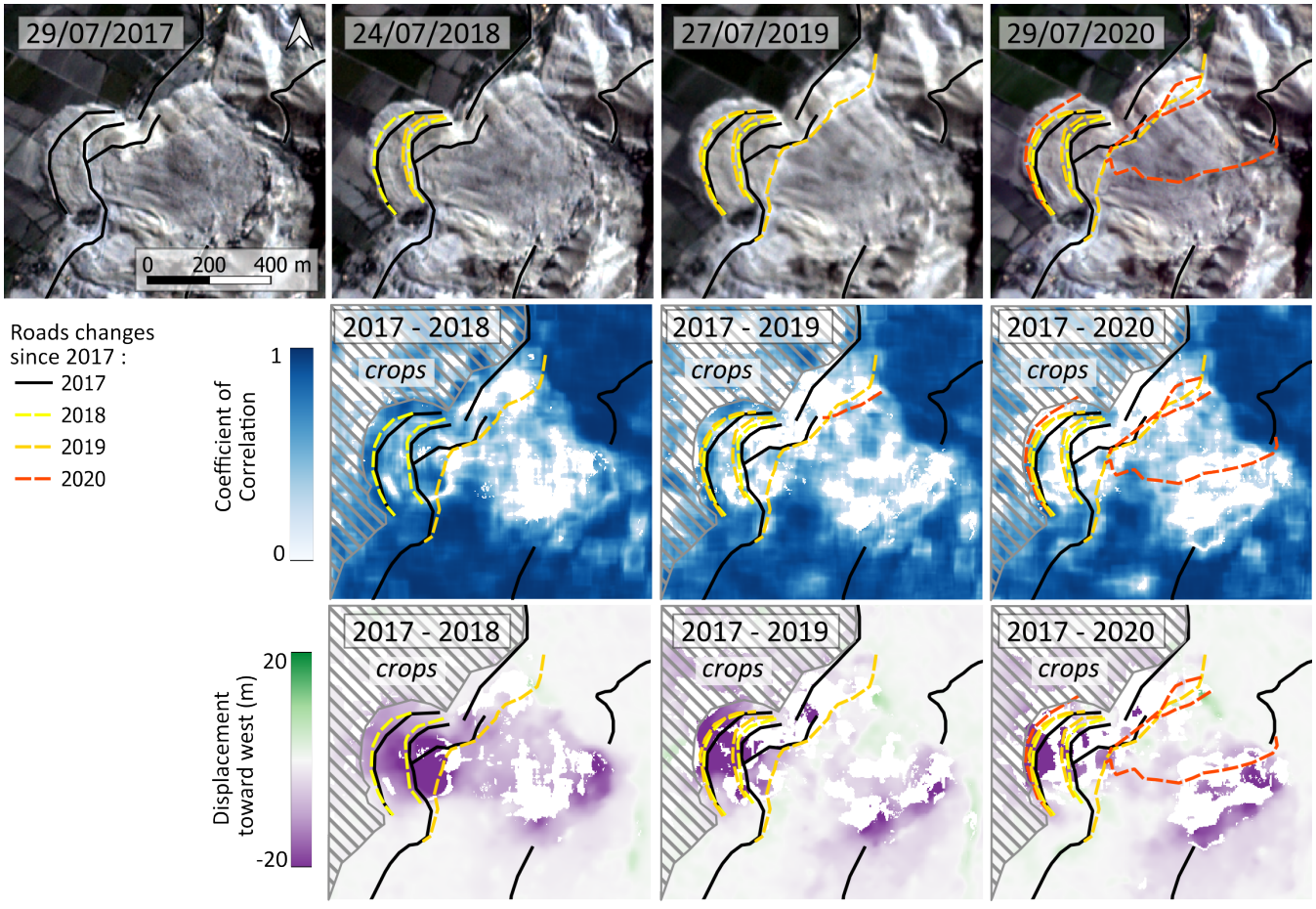


Figure 9. Impact of anthropogenic changes on the quality of correlation. First row shows PlanetScope images and changes on the roads over the years. Second row shows the evolution of coherence. We can see an increase in pixels with coherence under 0.2, especially in the central part, where the road has been changed. Third row shows the correlation after correction. The error increases as the two images are separated in time.

strategies, which include both long and short pairs, are also affected by errors associated with long-term pairs. However, the short-term pairs in these strategies do have an impact and help to reduce errors in the correlation. For Pie de la Cuesta, large movements combined with anthropogenic surface changes do not allow for a sufficient decrease in RMSE by adding short pairs. On the other hand, for Maca, the LST strategy performs slightly better than the LT strategy, notably due to better fitting of transient movements, which demonstrates the value of choosing this type of strategy when displacements are not too fast. Short temporal baseline pairs are valuable for capturing high-frequency signals and enhancing the spatial coherence of displacement fields, which is crucial for detecting transient phenomena and precursory motions (Lacroix et al., 2022, 2023). Conversely, longer temporal baseline pairs are better suited for detecting larger cumulative motions over time and can help in averaging out certain systematic errors, such as seasonal illumination effects.

https://doi.org/10.5194/egusphere-2026-6105
Preprint. Discussion started: 23 October 2026
© Author(s) 2026. CC BY 4.0 License.

4.2 New Insights into Landslide Processes through Improved Parameterization

Three parameterization factors were identified as having a significant impact on the results. First, the selection of images is crucial, as it strongly affects satellite-related errors. Second, the choice of the correlator significantly impacts the uncertainties. We were able to show that the MGM algorithm, thanks to its regularization parameter, reduces systematic errors in low-velocity areas. The BM algorithm, on the other hand, appears to perform better with high velocities but is more influenced by local variations. Third, the pairing strategy is essential to obtain accurate displacements. To map transient movements, strategies combining long and short pairs (LST) show better results. In contrast, strategies using only short pairs (ST) achieve greater consistency with very high velocities (several tens of meters per year). Eventually, the optimal configuration to obtain accurate displacements is the result of a balance between displacement accuracy, correlation robustness, temporal data sampling, and redundancy made possible by a careful parameterization throughout the complete workflow. We propose to illustrate what can be achieved through a carefully selected parameterization for three types of transient motions observed in slow-moving landslides in Peru.

4.2.1 Capturing River Erosion–Driven Landslide Acceleration: Maca Landslide

A pronounced and abrupt acceleration of the Maca landslide was observed in early March 2020, both in the GNSS permanent data and in the PlanetScope time-series (Figure 10). This acceleration has a different pattern than the acceleration caused by seasonal rainfalls, which initiates more smoothly (see, for instance, the acceleration in March 2021 or Bontemps et al. (2020)). In this case study, a large number of images around the acceleration period is essential to achieve the temporal resolution needed to detect the starting point of the acceleration. We chose MGM, which has shown the best results at low speeds, and combined it with a strategy involving short and long pairs (LST) to ensure consistency during both periods of low and high displacement. By choosing this strategy, we maximize the chances of achieving accurate displacement measurements before the acceleration, during the acceleration, and as the movement slows down. We analyzed the PlanetScope images, which show a localized collapse of a mass at the toe of the landslide (Figure 10), between February 28 and March 3. This mass collapse, which pushed the river toward the north by approximately 100 m, coincided with intense rainfall episodes and was triggered by fluvial erosion from the Colca River. The mechanisms linking fluvial erosion and slope activation are still largely understudied, except for extreme events like outburst floods (e.g., Cook et al. (2018)), despite having major impacts on long-term risk associated with fluvial erosion or on fluvial morphology. The mechanisms behind the slope activation might encompass both water seepage at the toe and river-bank erosion. The Maca landslide acceleration provides a unique opportunity to study these different mechanisms.

Displacement time-series extracted from eight representative points (MA1 to MA8) across the landslide body clearly illustrate a spatially variable kinematic response to this fluvial toe collapse. A longitudinal transect comprising points MA1, MA6, MA7, and MA8 (named T1) was extracted across the most active portion of the Maca landslide to evaluate the internal deformation pattern following the 2020 toe collapse. As shown in Figure 10, all four points exhibit nearly identical displacement

https://doi.org/10.5194/egusphere-2026-6105
Preprint. Discussion started: 23 October 2026
© Author(s) 2026. CC BY 4.0 License.

trajectories throughout the monitoring period, indicating that the entire lower landslide unit responded as a rigid block. The magnitude of the displacement during this transient movement was 10 m, much more than any annual movement recorded in Maca since the beginning of the monitoring period in 2012 (Zerathe et al., 2016; Bontemps et al., 2020). Therefore, it reinforces the idea that the landslide toe destabilization by river incision is a major driver of landslide activity at Maca. Furthermore, Maca is permanently in a subcritical state, which emphasizes the fact that even a small change in the system significantly affects the overall dynamics of the landslide.

A transect through the main slope and main displacement, comprising points MA1, MA2, MA3, MA4, and MA5 (named T2), was computed to evaluate the different times of response to the collapse of the toe and the way the different blocks of the landslide reacted to the movement. Until the toe collapse, the five points showed similar velocities, with a small seasonal oscillation due to differences in illumination. After the toe collapse, between 28/02/2020 and 03/03/2020, the points started to react differently. MA1 and MA5, located near the river, showed an immediate and pronounced response, following the same pattern as the first transect (T1). MA2 and MA3, situated in the upstream section of the landslide, between the secondary scarps, showed a more linear and less pronounced change in velocity than MA1 and MA5, which demonstrates a complex interaction between the two units of the landslide, with a damping of the motion further up. All four points have slowed down by the end of 2020 but have not totally stopped, showing the long-lasting effect of this mass collapse. These time-series show that the loss of mass of the slope triggers an instantaneous acceleration of the lower unit of the Maca landslide, which behaves as a rigid block, and propagates upward due to mechanical interactions between the different units. This analysis demonstrates the utility of high-frequency satellite-derived displacement time-series for identifying large-scale kinematic responses to localized destabilization events.

https://doi.org/10.5194/egusphere-2026-6105
Preprint. Discussion started: 23 October 2026
© Author(s) 2026. CC BY 4.0 License.

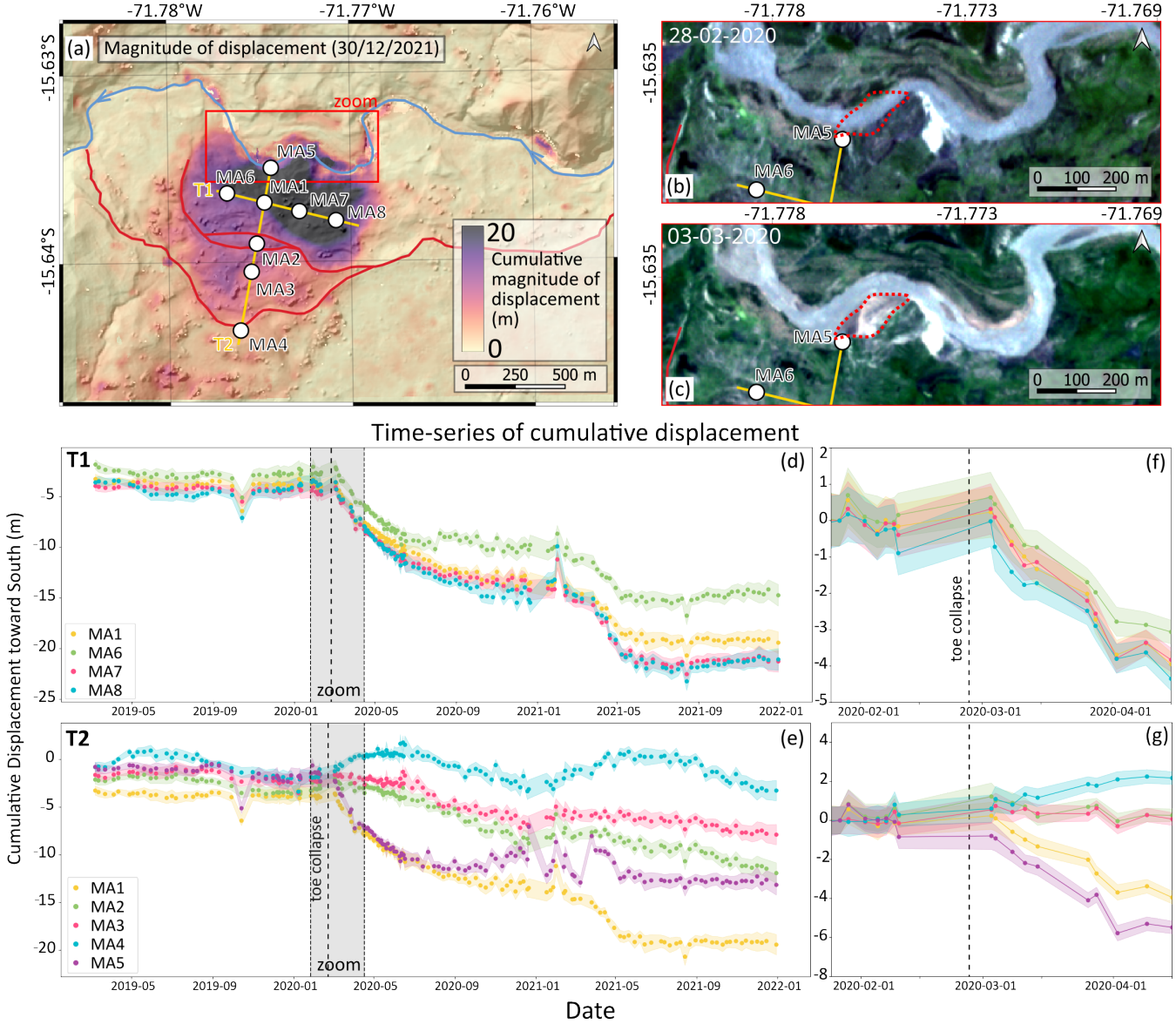


Figure 10. Relation between landslide motion and fluvial erosion on the Maca landslide. (a) Map of displacement magnitude between February 26, 2019 and December 30, 2021. Two displacement transects named T1 and T2 are used to analyze the displacement field. The red rectangle is the area zoomed in panels b and c. (b-c) PlanetScope images showing the evolution of the landslide toe on February 28, 2020, and March 3, 2020, highlighting the collapsed sector (around 0.8ha). (d) Displacement time-series, derived from PlanetScope, illustrating the kinematic response of points along a longitudinal profile following the toe collapse in early March 2020. (e) Displacement time-series (North-South component), extracted from upper to lower parts of the landslide (locations marked in (a)), illustrating the kinematic response to the river erosion, with a stronger movement at the toe. (f,g) Closer look at the acceleration of early 2020 for the two transects.

https://doi.org/10.5194/egusphere-2026-6105
Preprint. Discussion started: 23 October 2026
© Author(s) 2026. CC BY 4.0 License.

4.2.2 Capturing Material Supply–Driven Transient Accelerations in High-Velocity Landslides : Pie de la Cuesta Landslide

The Pie de la Cuesta landslide was active throughout the study period, from 2016 to 2025, and remains active to this day. As presented in Section 2.1.2, this landslide exhibits fairly high velocities (several tens of meters per year), involving rapid changes in morphological features. It is also influenced by human activity both in the moving areas and in the stable surrounding areas. The chosen strategy combines the MGM algorithm with a strategy based exclusively on short pairs (ST) to maximize consistency among correlated pairs. The large number of PlanetScope images available makes it easier to minimize the effect of morphological changes, which would have been harder to address using satellites with longer revisit times. The time-series of displacement shows two periods of transient acceleration, at the end of 2018 and in mid-2021. These accelerations can be particularly well detected at the fastest points of the landslide (e.g., TPC5). The arid environment of the area, combined with no evidence of a major precipitation event, excludes precipitation as the cause of these accelerations. We also discard seismic activity as their driver, since no earthquakes of magnitude greater than 4 were detected within 50 km of the landslide (https://ultimosismo.igp.gob.pe/productos/reportes-sismicos). On similar landslides in nearby areas, two previous studies show that accelerations are usually driven by material supplied to the moving mass due to headscarp retrogression (Lacroix et al., 2019, 2020a). Therefore, we also investigate this hypothesis and search for material supply from head- or secondary-scarp activity.

Optical imagery reveals morphological evidence of retrogressive activity, including escarpment retreat and block detachment between the end of June 2021 and the beginning of July 2021. This detachment, visible in Figure 11, affects a section of the secondary scarp. The secondary scarp can be seen as a block broke away and fell into the landslide mass. Displacement time-series from PlanetScope data, extracted from seven points across the landslide body (Figure 11) have been computed. The extraction points for the PlanetScope time-series were selected to correspond to different blocks of the landslide. TPC1 is located on the plateau in a stable area. TPC2 is situated between the main escarpment and the secondary escarpment. TPC3 is located on the secondary escarpment from which the block detached in late June 2021 (TPC4). TPC5 is situated in the area affected by the propagation of the block's detachment and in the high-velocity area. TPC6 and TPC7 are situated in the two frontal lobes of the landslide. The displacement time-series show at least two acceleration phases over the studied period, one occurring at the end of 2018 and the other in mid-2021. These accelerations were more pronounced in the central part of the landslide (transport zone, point TPC5) than toward the lobes (accumulation zone, TPC6 and TPC7), certainly caused by a steeper geometry of the internal shear zone and proximity to the driver origin.

https://doi.org/10.5194/egusphere-2026-6105
Preprint. Discussion started: 23 October 2026
© Author(s) 2026. CC BY 4.0 License.

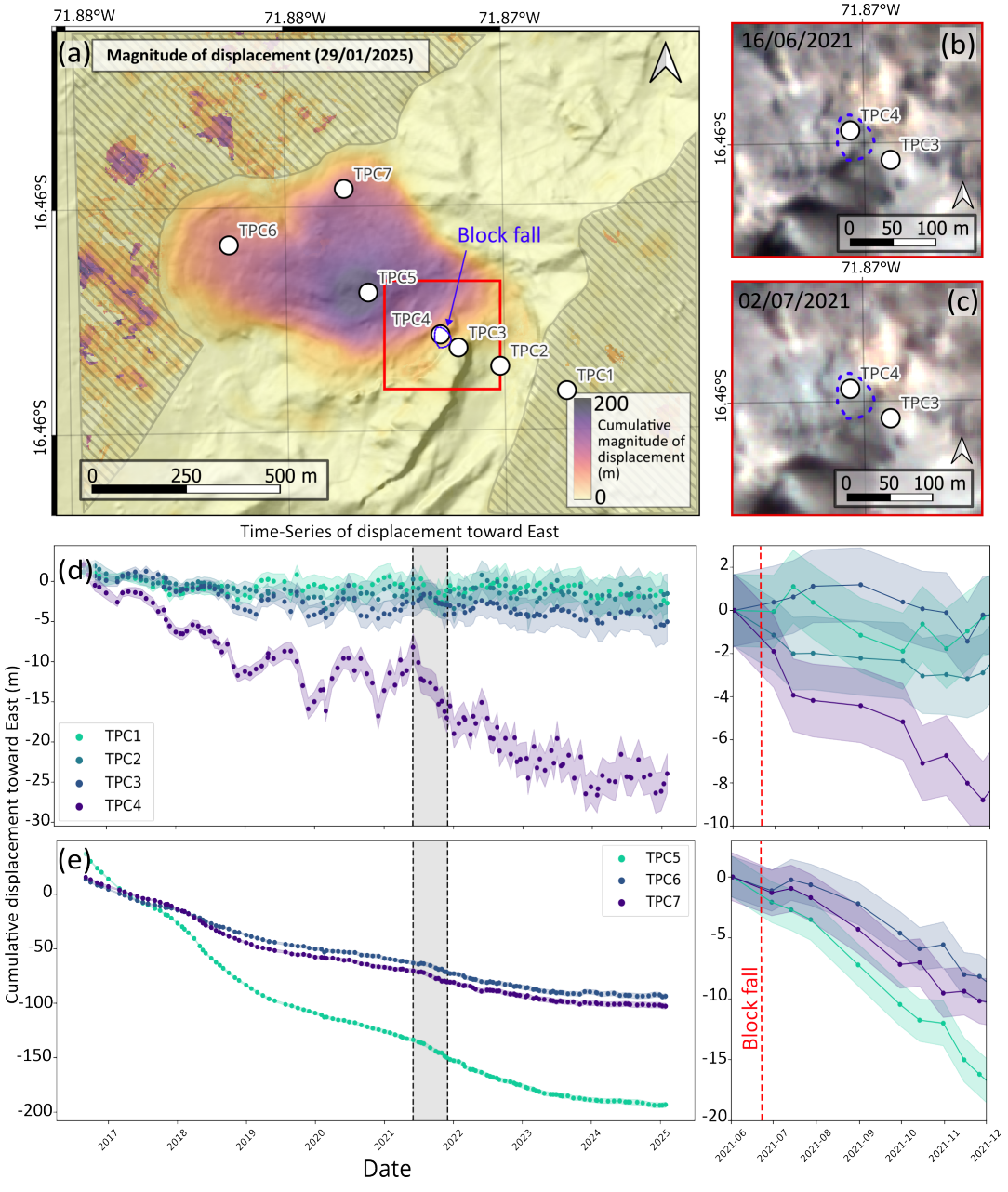


Figure 11. Secondary scarp retrogression and spatiotemporal displacement patterns across the Pie de la Cuesta landslide between July 17, 2016, and January 29, 2025. Map of cumulative displacement magnitude (a) obtained with the MGM-ST strategy, showing the PlanetScope points sampled and the area impacted by the block detachment (dashed line). These points were selected from different velocity zones within the landslide to distinguish the motion of individual blocks. Visual evidence of morphological evolution at the crown (b,c), including block detachment and crown retreat, as observed between November 25, 2016, and November 30, 2017. Time-series of cumulative displacement (d, e) for three points: TPC1, TPC2, and TPC7. TPC1 is located in a stable area on the plateau, TPC2 is situated between the two escarpments, and TPC7 is located where the secondary escarpment stretches, as shown in panels (b) and (c).

https://doi.org/10.5194/egusphere-2026-6105
Preprint. Discussion started: 23 October 2026
© Author(s) 2026. CC BY 4.0 License.

Points TPC1, TPC2, and TPC3 are located above the detaching block and show no acceleration. They are affected by a seasonal signal linked to illumination changes throughout the year. Point TPC4 is also strongly affected by a seasonal signal due to its position just below the secondary scarp, which can therefore cause significant shading effects. However, a long period of acceleration begins in June 2021. The points downstream of the detached block also show this same acceleration, potentially slightly later than at TPC4. Indeed, point TPC5 appears to begin accelerating in June 2021, but the points located within the lobes show an acceleration during July 2021, which may highlight the impact of the detached block on the downstream movement of the landslide.

On other similar landslides in the Vitor or Siguas valleys, these accelerations have been shown to be triggered by the retrogression of the headscarp, supplying new sediments to the landslide main body, modifying the hydrology, and accelerating the landslide motion in a transient way (Lacroix et al., 2019, 2020a). Further visual analysis of the PlanetScope imagery should be done to detect these scarp regressions. Further work should investigate the timing difference between the reactions of the different areas of the landslide to these regressions. This will be made possible by the great spatial density and high frequency of the PlanetScope satellite acquisitions.

4.2.3 Identifying the Co- and Post-seismic landslide movements: Cajabamba Landslide

At Cajabamba, observing both co-seismic and post-seismic displacements requires a short revisit time, since the response to co-seismic motion occurs within a few seconds, and post-seismic motion can last between days and several months. We use an event-centered strategy, employing long pairs to constrain the motion around the event and short pairs (LST) to precisely map the co- and post-seismic landslide response, coupled with the MGM algorithm.

The time-series of displacement on the Cajabamba landslide shows two periods of stability separated by a sudden acceleration initiated in May 2019, during or in the days after the Mw 8.0 Lagunas earthquake (Figure 12). This acceleration was noticeable on the surface due to damage to fields and buildings but was not recorded by instruments because the Cajabamba site was not monitored. This acceleration lasted about one month and was much larger at the toe of the landslide than in the upper part. This transient motion, measurable at the scale of the landslide, is one of the rare opportunities to study the mechanics of slow-moving landslides affected by earthquakes. Indeed, previous studies on slow-moving landslide acceleration during earthquakes have been based on either precise but very sparse GNSS time-series (Lacroix et al., 2014, e.g.), or medium-resolution imagery from Sentinel-1 (Lacroix et al., 2022; Cao et al., 2023), which prevents the detection of spatial variability in the landslide response to earthquakes. Despite the limitations of the previous studies, they have shown the combination of different mechanics in a co- or post-seismic period, including (1) stress increase during the shaking, (2) groundwater changes due to the shaking in the near-field of earthquakes with effects that can last from days to months, and (3) combined effects of damage and precipitation infiltration that can last up to several years. Here, we analyze the PlanetScope time-series on Cajabamba to supply a new case study to the short list of slow-moving landslides accelerated by earthquakes and analyze how it aligns with

https://doi.org/10.5194/egusphere-2026-6105
Preprint. Discussion started: 23 October 2026
© Author(s) 2026. CC BY 4.0 License.

previous findings.

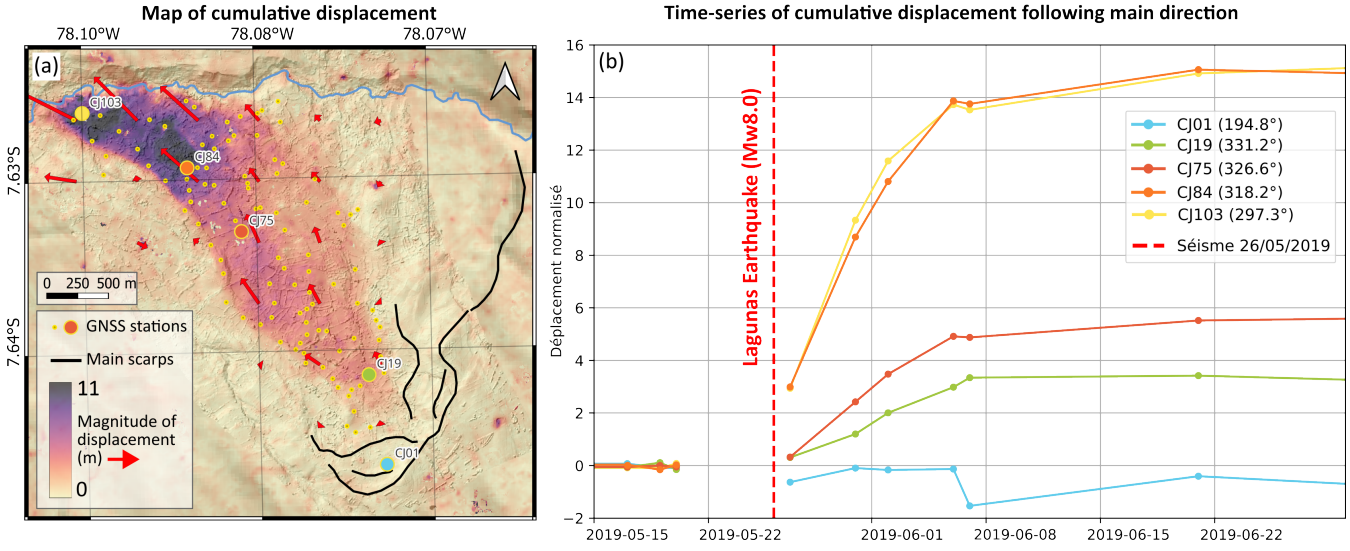


Figure 12. Acceleration of the Cajabamba landslide forced by the Lagunas earthquake on May 26, 2019. (a) Map showing the displacement field, extracted from PlanetScope images between June 15, 2017, and June 9, 2025, around the landslide area. The points correspond to five real GNSS measurement points recorded after the earthquake. They were used as reference locations for generating the PlanetScope time-series (b).

The landslide accumulated more than 14 m of displacement over 3 weeks (Figure 12) with larger motion close to the river-banks. The displacement fields show that the area affected by the acceleration was smaller than the total extent of the unstable zone, indicating that this acceleration did not affect the entire destabilized area. The latter is indicated in Figure 12, based on five GNSS points out of the 107 GNSS points available. CJ01 is located in a stable area, close to the main escarpment. CJ19 and CJ75 are in areas of moderate movement. Meanwhile, CJ84 and CJ103 are in high-velocity zones, particularly CJ103, the point closest to the river, at the toe of the landslide. These time-series clearly illustrate the post-seismic acceleration following the May 26, 2019, earthquake. Most of the movement is found at points CJ84 and CJ103, which are situated in the lower part of the landslide, where displacement exceeds 14 m. These two points clearly respond during or immediately after the earthquake. In contrast, the points further up, CJ19 and CJ75, appear to start responding a few days later, with almost zero co-seismic displacement.

The post-seismic movement lasted approximately one month, stabilizing around mid-June 2019. Before the earthquake, this landslide was relatively inactive, and it has since returned to a stable state, which shows that the movement at Cajabamba was almost entirely triggered by the earthquake. The return to initial conditions within three weeks is slightly more rapid compared to other monitored landslides, such as Maca, Tapgaon (Nepal), or those in New Zealand (Lacroix et al., 2022; Cao

https://doi.org/10.5194/egusphere-2026-6105
Preprint. Discussion started: 23 October 2026
© Author(s) 2026. CC BY 4.0 License.

et al., 2023). The analysis of the co- and post-seismic motion of the different units of the landslide suggests that the lower unit was activated first, both co- and post-seismically, and that the upper unit was activated in response to the release of stress caused by the movement of the lower unit. The PlanetScope time-series therefore brings new observations of the landslide unit interactions during earthquake forcings, which are usually limited by the low spatial and temporal resolution of previous satellite observations (Lacroix et al., 2022) and by the few GNSS points available to describe the spatial heterogeneity of the landslide velocity field. Finally, this short post-seismic period also highlights the value of using satellites such as PlanetScope to ensure sufficient data acquisition to capture the movement.

5 Conclusions

This study used PlanetScope optical satellite imagery to monitor slow-moving landslides, with a focus on improving displacement time-series through the evaluation of different strategies of pairwise image correlation and correlation algorithms, thanks to the validation of the results with independent in situ measurements on different landslides in Peru. The quality of the pairwise image correlation is profoundly impacted by both variations in illumination due to seasonal changes and the timing within the day of the acquisitions, as well as by the satellite's acquisition geometry. Mitigating these effects requires careful image pair selection with similar acquisition times and seasons. The correlation strategy has an important impact on the quality of the resulting displacement time-series. For rapidly moving landslides like Pie de la Cuesta (maximum 50 m/yr), short-term image pairing provides the best results, achieving a median RMSE of 1.01 m in the East-West (EW) direction and 1.18 m in the North-South (NS) direction for the MGM-ST strategy. Conversely, for slower landslides such as Maca (max 10 m/y), the More Global Matching Long and Short Term pairing (MGM-LST) improved the robustness and temporal resolution of displacement time-series, leading to median RMSE of 0.49 m in EW and 0.45 m in NS. The spatial quality of the displacement time-series is highly variable, driven mostly by morphological discontinuities and spatial heterogeneities of the landslide velocities. A key finding of our study is that uncertainties depend on the landslide velocity, calling into question the routine use of stable regions to estimate errors—a method traditionally employed in optical image correlation. The proposed workflow, available online, should incorporate in future work the correction of illumination bias, which is still the dominant source of error in the time-series.

These findings provide practical guidance for selecting appropriate image pairs for correlation analyses. The optimal temporal baseline depends on the dynamics of the investigated process. Short temporal baselines (ST) are particularly advantageous in areas experiencing high displacement rates or rapid morphological changes. In contrast, combining short and longer temporal baselines (LST) can provide complementary information for characterizing transient movements, accelerations, and potential precursors to fracturing. Overall, short pairs should be prioritized when rapid deformation is expected, whereas longer pairs can be used to capture more gradual or cumulative changes, provided that the associated increase in decorrelation remains acceptable.

https://doi.org/10.5194/egusphere-2026-6105
Preprint. Discussion started: 23 October 2026
© Author(s) 2026. CC BY 4.0 License.

The application of this workflow to three slow-moving landslides in Peru shows its ability to detect transient movements over time scales of a few days to a few weeks. These landslide transient movements are related to different forcings, including river erosion, earthquakes, and material supply from headscarp retrogression. The high temporal and spatial density of PlanetScope measurements provides insights into the mechanics of the landslides, showing the different timing and patterns of deformation of the different landslide units in response to these different forcings. Compared to other optical image satellites such as Sentinel-2 or Landsat, the analysis of transient movements, lasting only a few weeks, supports the use of PlanetScope, which remains unique as it provides up to one image per day along with high spatial resolution, enabling the study of bloc interactions a landslide. Regarding the applicability to other areas, our study focuses on the validation on two landslides with differences in steepness, velocity, vegetation cover. We believe this range is representative of a large proportion of landslides that are not covered by dense forest or by snow. The application of our workflow to detect and monitor transient acceleration could also open the door toward operational landslide monitoring of specific landslides in areas where cloud cover is not a limitation. To achieve this goal, automatic selection of PlanetScope images should first be developed, as download quotas exist and cloudy images strongly affect the results.

Code and data availability. The OCSlide workflow for PlanetScope images correlation and inversion used in this work is open-source (release under the GPL-3 license), publicly available and can be download from https://gricad-gitlab.univ-grenoble-alpes.fr/maurylau/ocslide. Running the complete workflow requires to install some dependencies (e.g. gdal, TIO AMES-Stereo-Pipeline) that are also freely available. The correlation of the optical images has been processed with AMES Stereo Pipeline Software publicly available, more information available in Beyer et al. (2018). Corrections of the output of correlation are done based on the work of Mueting and Bookhagen (2024) and Mueting et al. (2026). Inversion process is done following the code created by Bontemps et al. (2018) and available online: https://sourcesup.renater.fr/projects/tio/.

PlanetScope data can be accessed through Planet's Education and Research Program (Planet Team, 2026). The Pléiades DEMs have been obtained through Pléiades images provided by the DINAMIS/CNES program and can be ordered through the Airbus OneAtlas repository: https://space-solutions.airbus.com/imagery/how-to-order-imagery-and- data/.

Author contributions. LM conceptualized the data analysis workflow under the supervision of PL, performed the data analysis, and prepared the figures. LM wrote the manuscript based on the initial results produced by JH, with main contributions from PL. JH analysed the data, processed and formatted the GNSS datasets, and conducted the data quality assessment. LA and DG participated in the GNSS field data acquisition. SZ contributed to the interpretation of the results and provided substantial input to the manuscript. KD and FT participated to the workflow development with main contributions.

Competing interests. The authors declare that they have no conflict of interest.

https://doi.org/10.5194/egusphere-2026-6105
Preprint. Discussion started: 23 October 2026
© Author(s) 2026. CC BY 4.0 License.



Acknowledgements. The authors thank PlanetLab for providing access to the imagery through the Education and Research Program. The authors thanks INGEMMET for providing the GNSS data from the three study sites and the drone derived digital elevation model. The authors thank Kristen Cook who supervised Laureen Maury's work and the preparation of the manuscript.

https://doi.org/10.5194/egusphere-2026-6105
Preprint. Discussion started: 23 October 2026
© Author(s) 2026. CC BY 4.0 License.

References

Aati, S., Avouac, J.-P., Rupnik, E., and Deseilligny, M.-P.: Potential and Limitation of PlanetScope Images for 2-D and 3-D Earth Surface Monitoring With Example of Applications to Glaciers and Earthquakes, IEEE Transactions on Geoscience and Remote Sensing, 60, 1–19, https://doi.org/10.1109/TGRS.2022.3215821, 2022.

Beyer, R. A., Alexandrov, O., and McMichael, S.: The Ames Stereo Pipeline: NASA's Open Source Software for Deriving and Processing Terrain Data, Earth and Space Science, 5, 537–548, https://doi.org/10.1029/2018EA000409, _eprint: https://onlinelibrary.wiley.com/doi/pdf/10.1029/2018EA000409, 2018.

Bontemps, N., Lacroix, P., and Doin, M.-P.: Inversion of deformation fields time-series from optical images, and application to the long term kinematics of slow-moving landslides in Peru, Remote Sensing of Environment, 210, 144–158, https://doi.org/10.1016/j.rse.2018.02.023, 2018.

Bontemps, N., Lacroix, P., Larose, E., Jara, J., and Taipe, E.: Rain and small earthquakes maintain a slow-moving landslide in a persistent critical state, Nature Communications, 11, 780, https://doi.org/10.1038/s41467-020-14445-3, 2020.

Bradley, K., Mallick, R., Andikagumi, H., Hubbard, J., Meilianda, E., Switzer, A., Du, N., Brocard, G., Alfian, D., Benazir, B., Feng, G., Yun, S.-H., Majewski, J., Wei, S., and Hill, E. M.: Earthquake-triggered 2018 Palu Valley landslides enabled by wet rice cultivation, Nature Geoscience, 12, 935–939, https://doi.org/10.1038/s41561-019-0444-1, 2019.

Cao, Y., Hamling, I., Massey, C., and Upton, P.: Slow-Moving Landslides Triggered by the 2016 Mw 7.8 Kaikōura Earthquake, New Zealand: A New InSAR Phase-Gradient Based Time-Series Approach, Geophysical Research Letters, 50, e2022GL102 064, https://doi.org/10.1029/2022GL102064, _eprint: https://agupubs.onlinelibrary.wiley.com/doi/pdf/10.1029/2022GL102064, 2023.

Cook, K. L., Andermann, C., Gimbert, F., Adhikari, B. R., and Hovius, N.: Glacial lake outburst floods as drivers of fluvial erosion in the Himalaya, Science, 362, 53–57, https://doi.org/10.1126/science.aat4981, 2018.

Delacourt, C., Allemand, P., Casson, B., and Vadon, H.: Velocity field of the "La Clapière" landslide measured by the correlation of aerial and QuickBird satellite images, Geophysical Research Letters, 31, https://doi.org/10.1029/2004GL020193, _eprint: https://agupubs.onlinelibrary.wiley.com/doi/pdf/10.1029/2004GL020193, 2004.

Dille, A., Kervyn, F., Handwerger, A. L., d'Oreye, N., Derauw, D., Mugaruka Bibentyo, T., Samsonov, S., Malet, J.-P., Kervyn, M., and Dewitte, O.: When image correlation is needed: Unravelling the complex dynamics of a slow-moving landslide in the tropics with dense radar and optical time series, Remote Sensing of Environment, 258, 112 402, https://doi.org/10.1016/j.rse.2021.112402, 2021.

Facciolo, G., Franchis, C. D., and Meinhardt, E.: MGM: A Significantly More Global Matching for Stereovision, in: Procedings of the British Machine Vision Conference 2015, pp. 90.1–90.12, British Machine Vision Association, Swansea, ISBN 978-1-901725-53-7, https://doi.org/10.5244/C.29.90, 2015.

Feng, Z., Feng, G., Chen, H., Xu, W., Li, Z., He, L., and Ren, Z.: A Block Ramp Errors Correction Method of Planet Subpixel Offset: Application to the 2018 Mw 7.5 Palu Earthquake, Indonesia, IEEE Access, 7, 174 924–174 931, https://doi.org/10.1109/ACCESS.2019.2956198, 2019.

Frazier, A. E. and Hemingway, B. L.: A Technical Review of Planet Smallsat Data: Practical Considerations for Processing and Using PlanetScope Imagery, Remote Sensing, 13, 3930, https://doi.org/10.3390/rs13193930, number: 19, 2021.

Froude, M. J. and Petley, D. N.: Global fatal landslide occurrence from 2004 to 2016, Natural Hazards and Earth System Sciences, 18, 2161–2181, https://doi.org/10.5194/nhess-18-2161-2018, 2018.

https://doi.org/10.5194/egusphere-2026-6105
Preprint. Discussion started: 23 October 2026
© Author(s) 2026. CC BY 4.0 License.

Guzzetti, F., Mondini, A. C., Cardinali, M., Fiorucci, F., Santangelo, M., and Chang, K.-T.: Landslide inventory maps: New tools for an old problem, Earth-Science Reviews, 112, 42–66, https://doi.org/10.1016/j.earscirev.2012.02.001, 2012.

Handwerger, A. L., Lacroix, P., Bell, A. F., Booth, A. M., Huang, M.-H., Mudd, S. M., Bürgmann, R., and Fielding, E. J.: Multi-sensor remote sensing captures geometry and slow-to-fast sliding transition of the 2017 Mud Creek landslide, Scientific Reports, 15, 29 831, https://doi.org/10.1038/s41598-025-11399-8, 2025.

Hirschmüller, H.: Stereo processing by semiglobal matching and mutual information, IEEE transactions on pattern analysis and machine intelligence, 30, 328–341, https://doi.org/10.1109/TPAMI.2007.1166, 2008.

Huayllazo, Y., Infa, R., Soto, J., Lazarte, K., Huanca, J., Alvarez, Y., and Teixidó, T.: Using Electrical Resistivity Tomography Method to Determine the Inner 3D Geometry and the Main Runoff Directions of the Large Active Landslide of Pie de Cuesta in the Vítor Valley (Peru), Geosciences, 13, 342, https://doi.org/10.3390/geosciences13110342, 2023.

Hungr, O., Leroueil, S., and Picarelli, L.: The Varnes classification of landslide types, an update, Landslides, 11, 167–194, https://doi.org/10.1007/s10346-013-0436-y, 2014.

Infa, R., Chavez, A., Soto, J., Huanca, J., Roberti, G., Ward, B., Aguilar, R., and Teixidó, T.: Geological and Geomorphological Characterization of the Anthropogenic Landslide of Pie de la Cuesta in the Vitor Valley, Arequipa, Peru, Geosciences, 14, 291, https://doi.org/10.3390/geosciences14110291, 2024.

Instituto Geológico Minero y Metalúrgico: Monitoreo del Deslizamiento de Pie de la Cuesta 2022-2023, Caratula de Informe Tecnico A7507, Instituto Geológico Minero y Metalúrgico, Dirección de Geología Ambiental y Riesgo Geológico, https://sigrid.cenepred.gob.pe/sigridv3/documento/17718, 2024.

Intergovernmental Panel On Climate Change (Ipcc): The Ocean and Cryosphere in a Changing Climate: Special Report of the Intergovernmental Panel on Climate Change, Cambridge University Press, 1 edn., ISBN 978-1-009-15796-4 978-1-009-15797-1, https://doi.org/10.1017/9781009157964, 2022.

Intergovernmental Panel On Climate Change (Ipcc): Climate Change 2022 – Impacts, Adaptation and Vulnerability: Working Group II Contribution to the Sixth Assessment Report of the Intergovernmental Panel on Climate Change, Cambridge University Press, 1 edn., ISBN 978-1-009-32584-4, https://doi.org/10.1017/9781009325844, 2023.

Kääb, A., Altena, B., and Mascaro, J.: Coseismic displacements of the 14 November 2016 M_w 7.8 Kaikoura, New Zealand, earthquake using the Planet optical cubesat constellation, Natural Hazards and Earth System Sciences, 17, 627–639, https://doi.org/10.5194/nhess-17-627-2017, 2017.

Lacroix, P., Perfettini, H., Taipe, E., and Guillier, B.: Coseismic and postseismic motion of a landslide: Observations, modeling, and analogy with tectonic faults, Geophysical Research Letters, 41, 6676–6680, https://doi.org/10.1002/2014GL061170, _eprint: https://agupubs.onlinelibrary.wiley.com/doi/pdf/10.1002/2014GL061170, 2014.

Lacroix, P., Araujo, G., Hollingsworth, J., and Taipe, E.: Self-Entrainment Motion of a Slow-Moving Landslide Inferred From Landsat-8 Time Series, Journal of Geophysical Research: Earth Surface, 124, 1201–1216, https://doi.org/10.1029/2018JF004920, 2019.

Lacroix, P., Dehecq, A., and Taipe, E.: Irrigation-triggered landslides in a Peruvian desert caused by modern intensive farming, Nature Geoscience, 13, 56–60, https://doi.org/10.1038/s41561-019-0500-x, 2020a.

Lacroix, P., Handwerger, A. L., and Bièvre, G.: Life and death of slow-moving landslides, Nature Reviews Earth & Environment, 1, 404–419, https://doi.org/10.1038/s43017-020-0072-8, 2020b.

https://doi.org/10.5194/egusphere-2026-6105
Preprint. Discussion started: 23 October 2026
© Author(s) 2026. CC BY 4.0 License.

Lacroix, P., Gavillon, T., Bouchant, C., Lavé, J., Mugnier, J.-L., Dhungel, S., and Vernier, F.: SAR and optical images correlation illuminates post-seismic landslide motion after the Mw 7.8 Gorkha earthquake (Nepal), Scientific Reports, 12, 6266, https://doi.org/10.1038/s41598-022-10016-2, 2022.

Lacroix, P., Huanca, J., Albinez, L., and Taipe, E.: Precursory Motion and Time-Of-Failure Prediction of the Achoma Landslide, Peru, From High Frequency PlanetScope Satellites, Geophysical Research Letters, 50, e2023GL105 413, https://doi.org/10.1029/2023GL105413, _eprint: https://onlinelibrary.wiley.com/doi/pdf/10.1029/2023GL105413, 2023.

Leprince, S., Muse, P., and Avouac, J.-P.: In-Flight CCD Distortion Calibration for Pushbroom Satellites Based on Subpixel Correlation, IEEE Transactions on Geoscience and Remote Sensing, 46, 2675–2683, https://doi.org/10.1109/TGRS.2008.918649, 2008.

Mazzanti, P., Caporossi, P., and Muzi, R.: Sliding Time Master Digital Image Correlation Analyses of CubeSat Images for landslide Monitoring: The Rattlesnake Hills Landslide (USA), Remote Sensing, 12, 592, https://doi.org/10.3390/rs12040592, 2020.

Mueting, A. and Bookhagen, B.: Tracking slow-moving landslides with PlanetScope data: new perspectives on the satellite's perspective, Earth Surface Dynamics, 12, 1121–1143, https://doi.org/10.5194/esurf-12-1121-2024, 2024.

Mueting, A., Charrier, L., and Bookhagen, B.: Challenges in reconstructing seasonally driven landslide motion from optical satellite data: insights from the Del Medio catchment, NW Argentina, EGUsphere, pp. 1–28, https://doi.org/10.5194/egusphere-2025-6445, 2026.

Mölder, F., Jablonski, K. P., Letcher, B., Hall, M. B., Van Dyken, P. C., Tomkins-Tinch, C. H., Sochat, V., Forster, J., Vieira, F. G., Meesters, C., Lee, S., Twardziok, S. O., Kanitz, A., VanCampen, J., Malladi, V., Wilm, A., Holtgrewe, M., Rahmann, S., Nahnsen, S., and Köster, J.: Sustainable data analysis with Snakemake, F1000Research, 10, 33, https://doi.org/10.12688/f1000research.29032.3, 2025.

Narcisi, R., Pappalardo, S. E., Taddia, G., and De Marchi, M.: Assessing climate impacts on slow-moving landslides in the western Alps of Piemonte: integration of monitoring techniques for detecting displacements, Frontiers in Earth Science, 12, https://doi.org/10.3389/feart.2024.1365469, 2024.

Nunez Juarez, S. A. and Chacaltana Budiel, C. A.: Evaluacion de Peligros por Deslizamientos en los Centros Poblados Colcas y Nunumabamba, Informe Tecnico N°A7047, Direccion de Geologica Ambiental y Riesgo Geologico, https://sigrid.cenepred.gob.pe/sigridv3/documento/9756, 2020.

Pham, M. Q., Lacroix, P., and Doin, M. P.: Sparsity Optimization Method for Slow-Moving Landslides Detection in Satellite Image Time-Series, IEEE Transactions on Geoscience and Remote Sensing, 57, 2133–2144, https://doi.org/10.1109/TGRS.2018.2871550, 2019.

Planet Team: Planet Application Program Interface: In Space for Life on Earth, San Francisco, CA, https://api.planet.com, 2026.

Provost, F., Michéa, D., Malet, J.-P., Boissier, E., Pointal, E., Stumpf, A., Pacini, F., Doin, M.-P., Lacroix, P., Proy, C., and Bally, P.: Terrain deformation measurements from optical satellite imagery: The MPIC-OPT processing services for geohazards monitoring, Remote Sensing of Environment, 274, 112 949, https://doi.org/10.1016/j.rse.2022.112949, 2022.

Purinton, B., Mueting, A., and Bookhagen, B.: Image Texture as Quality Indicator for Optical DEM Generation: Geomorphic Applications in the Arid Central Andes, Remote Sensing, 15, 85, https://doi.org/10.3390/rs15010085, 2023.

Roy, D. P., Huang, H., Houborg, R., and Martins, V. S.: A global analysis of the temporal availability of PlanetScope high spatial resolution multi-spectral imagery, Remote Sensing of Environment, 264, 112 586, https://doi.org/10.1016/j.rse.2021.112586, 2021.

Shean, D. E., Alexandrov, O., Moratto, Z. M., Smith, B. E., Joughin, I. R., Porter, C., and Morin, P.: An automated, open-source pipeline for mass production of digital elevation models (DEMs) from very-high-resolution commercial stereo satellite imagery, ISPRS Journal of Photogrammetry and Remote Sensing, 116, 101–117, https://doi.org/10.1016/j.isprsjprs.2016.03.012, 2016.

Stumpf, A., Malet, J.-P., and Delacourt, C.: Correlation of satellite image time-series for the detection and monitoring of slow-moving landslides, Remote Sensing of Environment, 189, 40–55, https://doi.org/10.1016/j.rse.2016.11.007, 2017.

https://doi.org/10.5194/egusphere-2026-6105
Preprint. Discussion started: 23 October 2026
© Author(s) 2026. CC BY 4.0 License.



Thouret, J. C., Wörner, G., Gunnell, Y., Singer, B., Zhang, X., and Souriot, T.: Geochronologic and stratigraphic constraints on canyon incision and Miocene uplift of the Central Andes in Peru, Earth and Planetary Science Letters, 263, 151–166, https://doi.org/10.1016/j.epsl.2007.07.023, 2007.

Vallée, M., Xie, Y., Grandin, R., Villegas-Lanza, J. C., Nocquet, J.-M., Vaca, S., Meng, L., Ampuero, J. P., Mothes, P., Jarrin, P., Sierra Farfán, C., and Rolandone, F.: Self-reactivated rupture during the 2019 *M*w=8 northern Peru intraslab earthquake, Earth and Planetary Science Letters, 601, 117 886, https://doi.org/10.1016/j.epsl.2022.117886, 2023.

Vargas Vilchez, L.: Geología del cuadrángulo de Arequipa - [Boletín A 24], Instituto Geológico, Minero y Metalúrgico - INGEMMET, https://repositorio.ingemmet.gob.pe/handle/20.500.12544/142, accepted: 2013-01-18T21:44:06Z, 1970.

Zerathe, S., Lacroix, P., Jongmans, D., Marino, J., Taipe, E., Wathelet, M., Pari, W., Smoll, L. F., Norabuena, E., Guillier, B., and Tatard, L.: Morphology, structure and kinematics of a rainfall controlled slow-moving Andean landslide, Peru, Earth Surface Processes and Landforms, 41, 1477–1493, https://doi.org/10.1002/esp.3913, _eprint: https://onlinelibrary.wiley.com/doi/pdf/10.1002/esp.3913, 2016.